The Astrophysical Journal, 976:196 (14pp), 2024 December 1 https://doi.org/10.3847/1538-4357/ad83be

Expanding the Inventory of Molecule-rich Planetary Nebulae: New Observations of M4-17, Hu 1-1, M1-59, and Na 2

K. R. Gold[1], D. R. Schmidt[2], and L. M. Ziurys[1,3]
[1] Department of Chemistry and Biochemistry, University of Arizona, PO Box 210041, Tucson, AZ 85721-0041, USA; lziurys@arizona.edu
[2] Department of Physics and Astronomy, Franklin & Marshall College, PO Box 3003, Lancaster, PA 17604-3003, USA
[3] Department of Astronomy, Arizona Radio Observatory, and Steward Observatory, University of Arizona, 933 N. Cherry Avenue, Tucson, AZ 85721-0065, USA
Received 2024 September 4; revised 2024 October 3; accepted 2024 October 4; published 2024 November 22

Abstract

Molecular observations of four planetary nebulae (PNe), M4-17, Hu 1-1, M1-59, and Na 2, were conducted at 1–3 mm using the Arizona Radio Observatory's 12 m antenna and Submillimeter Telescope, and the Institut de Radioastronomie Millimétrique 30 m Telescope. Toward M4-17, HNC ($J = 3 \rightarrow 2$), CCH ($N = 2 \rightarrow 1$, $N = 3 \rightarrow 2$), CN ($N = 1 \rightarrow 0$, $N = 2 \rightarrow 1$), H_2CO ($J_{Ka,Kc} = 2_{1,2} \rightarrow 1_{1,1}$, $J_{Ka,Kc} = 2_{0,2} \rightarrow 1_{0,1}$, $J_{Ka,Kc} = 2_{1,1} \rightarrow 1_{1,0}$), CS ($J = 3 \rightarrow 2$, $J = 5 \rightarrow 4$), and $H^{13}CN$ ($J = 2 \rightarrow 1$) were detected. An almost identical set of transitions was identified toward Hu 1-1. Moreover, c–C_3H_2 was detected in Hu 1-1 via three 2 mm lines: $J_{Ka,Kc} = 3_{1,2} \rightarrow 2_{2,1}$, $J_{Ka,Kc} = 4_{1,4} \rightarrow 3_{0,3}$, and $J_{Ka,Kc} = 3_{2,2} \rightarrow 2_{1,1}$. HNC, CCH, CN, CS, and $H^{13}CN$ were found in M1-59, as well as H_2S via its $J_{Ka,Kc} = 1_{1,0} \rightarrow 1_{0,1}$ line—the first detection of this key sulfur species in PNe. In addition, CCH and CN were identified in the 27,000 yr old Na 2. Among these four sources, CN and CCH were the most prevalent molecules (after CO and H_2) with fractional abundances, relative to H_2, of $f \sim 0.9$–7.5×10^{-7} and 0.8–7.5×10^{-7}, respectively. CS and HNC have abundances in the range $f \sim 0.5$–5×10^{-8}, the latter resulting in HCN/HNC ~ 3 across all three PNe. The unusual species H_2CO, c–C_3H_2, and H_2S had $f \sim 3$–4×10^{-7}, 10^{-8}, and 6×10^{-8}. This study suggests that elliptical PNe such as Hu 1-1 can have a diverse molecular composition. The presence of CN, CCH, and HCO^+ in Na 2, with comparable abundances to younger PNe, demonstrates that molecular content is maintained into the late PN stage.

Unified Astronomy Thesaurus concepts: Astrochemistry (75); Interstellar molecules (849); Planetary nebulae (1249); Radio astronomy (1338); Molecular spectroscopy (2095)

1. Introduction

Planetary nebulae (PNe) represent the final phase in the evolution of low- to intermediate-mass stars, with progenitor masses ranging from ∼0.8 to 8 $M_\odot$ (I. Iben & A. Renzini 1983). During the asymptotic giant branch (AGB) phase, significant mass loss results in the formation of a generally spherical circumstellar envelope. This envelope later evolves into the diverse morphologies observed in PNe, from elliptical to bipolar to multipolar (B. Balick & A. Frank 2002). During the transition at the end of the AGB, the object's outer layers are expelled, exposing the hot carbon–oxygen core. Once the core's surface temperature reaches 30,000 K, strong ultraviolet (UV) radiation from the star ionizes the ejected material, forming a planetary nebula.

Such ionization in PNe led to the belief that any molecular content would be largely photodissociated, with only atomic and diatomic species remaining from the molecule-rich AGB envelope. Models (M. P. Redman et al. 2003; R. K. Kimura et al. 2012) of the chemical evolution of PNe predict a significant decline in gas-phase molecular abundances over the nebular lifetime, despite shielding within dusty clumps. For example, the HCN abundance falls by ∼7 orders of magnitude between 2000 and 10,000 yr (M. P. Redman et al. 2003). Consequently, planetary nebulae were largely perceived as atomic entities, with molecular studies primarily focused on CO (e.g., P. J. Huggins & A. P. Healy 1989; P. J. Huggins et al. 1996, 2005).

Over the past decades, observations have clearly demonstrated that some PNe possess a far richer molecular composition than speculated by theoretical models. Earlier work showed that CN, HCN, HNC, and HCO^+ were present in a few PNe, including the very old Helix Nebula (NGC 7293; one position) and NGC 6072 (P. Cox et al. 1992; R. Bachiller et al. 1997). Furthermore, Y. Zhang et al. (2008) identified a range of species in the young PN NGC 7027, such as N_2H^+, c–C_3H_2, and HC_3N. More recent studies show that polyatomic molecules are present throughout the Helix, which has an estimated age of ∼12,000 yr; HCO^+, H_2CO, CCH, c–C_3H_2, HNC, and HCN were detected at multiple positions across the nebula (L. N. Zack & L. M. Ziurys 2013; N. R. Zeigler et al. 2013; D. R. Schmidt & L. M. Ziurys 2017a; D. R. Schmidt et al. 2018a). Additionally, J. L. Edwards & L. M. Ziurys (2013, 2014) and J. L. Edwards et al. (2014) identified numerous species in the young PN NGC 6537 (Red Spider Nebula) and in the middle-aged source M2-48, such as CN, HCN, HNC, CS, SO, H_2CO, HCO^+, and N_2H^+. D. R. Schmidt & L. M. Ziurys (2016, 2017a, 2017b) then conducted surveys of HCN, HCO^+, HNC, and CCH in a sample of 17 PNe, the so-called "Level 1" objects, with a detection rate of ∼75%–90%. The young PN K4-47 was found to contain some of the most complex molecules to date in these objects: CH_3CN, CH_3CCH, and CH_2NH (D. R. Schmidt & L. M. Ziurys 2019). Chemical complexity reached a pinnacle in the identification of C_{60} and C_{70} in several PNe, such as Tc-1 (J. Cami et al. 2010; D. A. García-Hernández et al. 2010, 2011, 2012; M. Otsuka et al. 2013). Overall, these works, with a focus on HCN, HNC,

CS, and HCO^+, have provided evidence that molecular abundances do not vary significantly with PN age across a 12,000 yr lifespan (J. L. Edwards et al. 2014; D. R. Schmidt & L. M. Ziurys 2016, 2017a, 2017b).

Very recently, D. R. Schmidt et al. (2022) expanded their survey work to include 13 new PNe, so-called "Level 2" objects, characterized by slightly weaker CO ($J = 2 \rightarrow 1$) emission (P. J. Huggins & A. P. Healy 1989; P. J. Huggins et al. 1996, 2005), as compared to the "Level 1" sources. This new set encompassed nebulae with ages ranging from ~2000 to over 25,000 yr and exhibiting various morphologies. HCN and HCO^+ were detected in 10 of these nebulae: He 2–459, Hu 1-1, K3-52, K3-65, M1-8, M1-40, M1-59, M2-53, M4-17, and NGC 6445. In addition to these, the oldest source in the set, Na 2, was found to contain HCO^+ (D. R. Schmidt et al. 2022). These detections lent further support to the concept that polyatomic molecules are common constituents in PNe of various ages and morphologies.

In order to examine trends in molecular abundances for species beyond HCN and HCO^+, further observational studies have been conducted of four of the Level 2 sources: M4-17, Hu 1-1, M1-59, and Na 2. The selection of these sources was based on their distinctive morphologies and age. Na 2 is exceptionally old at ~27,000 yr. M1-59 and M4-17 display complex bipolar/multipolar morphologies, whereas Hu 1-1 is characterized as elliptical. Using the combination of the facilities of the Arizona Radio Observatory (ARO) and the Institut de Radioastronomie Millimétrique (IRAM) 30 m, detections were made of CN, CS, CCH, H_2CO, HNC, and c–C_3H_2 among the four sources, and the first identification of H_2S in PNe, found in M1-59. $H^{13}CN$ was also detected in Hu 1-1, M4-17, and M1-59, expanding the work of L. M. Ziurys et al. (2020) on the measurement of $^{12}C/^{13}C$ ratios in PNe. In this paper, we present our observational results for these four nebulae and an analysis of their molecular abundances. We then comment on their overall implications for the chemistry in PNe.

2. Observations

Observations of M4-17, Hu 1-1, M1-59, and Na 2 were carried out using three facilities: the ARO 12 m antenna at Kitt Peak, Arizona, operating at 2 and 3 mm, the ARO Submillimeter Telescope (SMT) at Mount Graham, Arizona, for 1 mm measurements, and the IRAM 30 m at Pico Veleta, Spain at 2 mm. The ARO data were collected between 2021 March and 2024 June, while the 30 m measurements were conducted from 2021 May through 2023 January.

For the 12 m antenna observations, dual-polarization 2 and 3 mm receivers, employing sideband-separating (SBS) mixers, were used. Image rejection, intrinsic to the mixer design, generally exceeded 20 dB. The ARO Wideband Spectrometer (AROWS) served as the backend, configured to a spectral resolution of 625 kHz with 4–8 GHz of instantaneous bandwidth. Beam sizes ranged from 36″ to 71″ with beam efficiencies (η_B) between 0.76 and 0.92; see Table 1. System temperatures typically varied between 120 and 350 K. Data were taken in beam-switching mode with a subreflector throw of ±2′ for all sources.

At the SMT, a dual-polarization 1.3 mm receiver was employed, consisting of ALMA Band 6 SBS mixers. For these observations, a 2048-channel filter bank with 1 MHz resolution functioned as the primary backend. Image rejection levels were typically >15 dB. Beam sizes were between 28″ and 33″, and beam efficiencies ranged from 0.66 to 0.70 (Table 1). System temperatures were generally in the 200–275 K range. Data were taken in beam-switching mode with a subreflector throw of ±2′ for all sources.

At the IRAM 30 m, the Eight MIxer Receiver (EMIR) E150 band, equipped with dual-polarization SIS mixers, was used in conjunction with the Fast Fourier Transform Spectrometers (FTS) backend with a channel resolution of 200 kHz. This configuration provided 16 GHz of simultaneous bandwidth per polarization, divided equally between two frequency windows. The wideband correlator WILMA served as the secondary backend with reduced resolution (2 MHz per channel). Beam sizes ranged from 14″ to 17″, with beam efficiencies between 0.68 and 0.73 (Table 1). System temperatures were typically between 120 and 225 K. Observations used the wobbler switching mode with a ±40″ offset.

All measurements were conducted on the T_A^* temperature scale. Calibration was performed using the chopper wheel method. Antenna temperature was converted to radiation temperature (T_R) using the expression $T_R = T_A^*/\eta_B$, where η_B represents the beam efficiency (see Table 1). To evaluate image contamination, a local oscillator shift of 20 MHz was implemented at all facilities and frequencies. Pointing and focus were checked every 1–2 hr using strong continuum sources or with spectral line pointing (IRC+10216). Typical pointing corrections were less than 5″. Integration times were between 4 and 90 hr, depending on the frequency setting.

Table 1 details the observed line frequencies at each telescope, along with the corresponding beam sizes and efficiencies. Table 2 lists the four PNe and their coordinates, angular size, distance, morphology, estimated age, central star temperature, and if it is a known source of H_2 emission. All data were averaged using the Continuum and Line Analysis Single-dish Software (CLASS).[4] When necessary, a low-order baseline was removed.

3. Results

Optical images of the four PNe studied in this work, M4-17, Hu 1-1, M 1-59, and Na 2, are shown in Figure 1. Spectra of the molecules detected in these objects are displayed in Figures 2–5. The telescope used for each line is given in the respective tables, but is also indicated on the figure when the same line was observed at two telescopes. Molecular identifications were generally based on at least two observed transitions per species, or via fine/hyperfine structure. The fine-structure spin–rotation doublets, indicated by quantum number J, were observed for the transitions of CN and CCH, which both have $^2\Sigma^+$ ground states. In these cases, the rotational quantum number is N. These two molecules also have hyperfine structure, and while such splittings were not resolved given the observed line widths, they did broaden the spectra. Line intensities ranged from 0.8 to 24 mK over the four sources.

All spectra were fitted with Gaussian curves to determine peak line intensities (T_A^*), full width at half maximum line widths ($\Delta v_{1/2}$), and LSR velocities (V_{LSR}). For CCH and CN, individual fine-structure components were fit in the analysis. The resulting line parameters are presented in Tables 3–6, in the order M4-17, Hu 1-1, M1-59, and Na 2. The results for the individual sources are discussed below.

[4] https://www.iram.fr/IRAMFR/GILDAS/

Table 1
Transition Frequencies and Telescope Parameters

Molecule	Transition	Frequency (MHz)	Telescope	θ_B (arcsec)	η_B
CO	$J = 1 \rightarrow 0$	115,271.2018	12 m	55	0.86
HCN	$J = 1 \rightarrow 0$[a]	88,631.6022	12 m	71	0.92
	$J = 3 \rightarrow 2$	265,886.4339	SMT	28	0.67
$H^{13}CN$	$J = 2 \rightarrow 1$	172,677.8512	IRAM	14	0.68
HCO^+	$J = 1 \rightarrow 0$	89,188.5247	12 m	70	0.92
	$J = 3 \rightarrow 2$	267,557.6259	SMT	28	0.67
HNC	$J = 1 \rightarrow 0$	90,663.5680	12 m	69	0.91
	$J = 3 \rightarrow 2$	271,981.1420	SMT	28	0.67
CN	$N_J = 1_{1/2} \rightarrow 0_{1/2}$[b]	113,191.2787	12 m	56	0.86
	$N_J = 1_{3/2} \rightarrow 0_{1/2}$[a]	113,490.9702	12 m	55	0.86
	$N_J = 2_{3/2} \rightarrow 1_{1/2}$[a]	226,659.5584	SMT	33	0.70
	$N_J = 2_{5/2} \rightarrow 1_{3/2}$[a]	226,874.7813	SMT	33	0.70
CCH	$N_J = 2_{5/2} \rightarrow 1_{3/2}$[a]	174,663.1990	12 m	36	0.76
			IRAM	14	0.68
	$N_J = 2_{3/2} \rightarrow 1_{1/2}$[a]	174,721.7440	12 m	36	0.76
			IRAM	14	0.68
	$N_J = 3_{7/2} \rightarrow 2_{5/2}$[a]	262,004.2600	SMT	29	0.66
	$N_J = 3_{5/2} \rightarrow 2_{3/2}$[a]	262,064.9860	SMT	29	0.66
c–C_3H_2	$J_{Ka,Kc} = 3_{1,2} \rightarrow 2_{2,1}$	145,089.6055	IRAM	17	0.73
	$J_{Ka,Kc} = 4_{1,4} \rightarrow 3_{0,3}$	150,851.9080	IRAM	16	0.72
	$J_{Ka,Kc} = 3_{2,2} \rightarrow 2_{1,1}$	155,518.3032	IRAM	15	0.71
CS	$J = 2 \rightarrow 1$	97,980.9533	12 m	64	0.90
	$J = 3 \rightarrow 2$	146,969.0287	IRAM	16	0.72
	$J = 5 \rightarrow 4$	244,935.5565	SMT	31	0.66
H_2S	$J_{Ka,Kc} = 1_{1,0} \rightarrow 1_{0,1}$	168,762.7624	IRAM	14	0.69
H_2CO	$J_{Ka,Kc} = 2_{1,2} \rightarrow 1_{1,1}$	140,839.5020	12 m	45	0.80
	$J_{Ka,Kc} = 2_{0,2} \rightarrow 1_{0,1}$	145,602.9490	IRAM	17	0.73
	$J_{Ka,Kc} = 2_{1,1} \rightarrow 1_{1,0}$	150,498.3340	12 m	42	0.79
			IRAM	16	0.72

Notes.
[a] Blend of hyperfine components.
[b] Strongest hyperfine component.

M4-17: This planetary nebula, located at a distance of 2.2 kpc (M. A. Guerrero et al. 2000), has an extended central region about 20″ in size and a less-defined bipolar outflow, as deduced from [N II] and 2 μm H_2 images (A. Manchado et al. 1996; M. A. Guerrero et al. 2000). The nebula has a kinematic age of approximately 9000 yr, derived from its distance, and an expansion velocity of 17 km s^{-1}. The central star temperature is approximately 127,000 K (L. Stanghellini et al. 2002). The H_2 emission appears to be concentrated in the central region (M. A. Guerrero et al. 2000) but also appears in the bipolar lobes. Comparison of the CCH and H_2CO 12 m and IRAM data suggests a source size of ∼30″ for this PN, consistent with the full H_2 image.

D. R. Schmidt et al. (2022) observed the $J = 1 \rightarrow 0$ and $J = 3 \rightarrow 2$ transitions of both HCN and HCO^+ in M4-17, as well as the $J = 1 \rightarrow 0$ and $J = 2 \rightarrow 1$ lines of CO. P. J. Huggins et al. (2005) had previously found the $J = 2 \rightarrow 1$ transition of CO. As shown in Figure 2, CN, CCH, CS, H_2CO, and HNC have been newly detected in this source, along with a line of $H^{13}CN$. Two lines of CS were measured ($J = 3 \rightarrow 2$ and $J = 5 \rightarrow 4$), and three of H_2CO ($J_{Ka,Kc} = 2_{1,2} \rightarrow 1_{1,1}$, $J_{Ka,Kc} = 2_{0,2} \rightarrow 1_{0,1}$ and $J_{Ka,Kc} = 2_{1,1} \rightarrow 1_{1,0}$), one at both the 12 m and the 30 m (see Table 3). In addition, two transitions each of CN ($N = 1 \rightarrow 0$ and $N = 2 \rightarrow 1$) and CCH ($N = 2 \rightarrow 1$ and $N = 3 \rightarrow 2$) were detected, each consisting of two spin–rotation components, indicated by quantum number J. The intensity ratios of the spin–rotation components are marked under the spectra. The $J = 3 \rightarrow 2$ transition of HNC and the $J = 2 \rightarrow 1$ line of $H^{13}CN$ were identified as well. In addition, the signal-to-noise ratios were improved for the HCN and HCO^+ : $J = 1 \rightarrow 0$ and $J = 3 \rightarrow 2$ lines, as well as for the CO: $J = 1 \rightarrow 0$ transition. These refined spectra are also presented in Figure 2.

As shown in Table 3, the average LSR velocity is -5.8 ± 4.0 km s^{-1} with typical line widths near 30–35 km s^{-1}, consistent with previous measurements (D. R. Schmidt et al. 2022). Some lines appear broader due to blended hyperfine structure (e.g., CN, CCH). The intensities are typically 4–10 mK, with the strongest features from CO and CN.

Hu 1-1: This planetary nebula is thought to exhibit an elliptical morphology with some asymmetry (A. Manchado et al. 1996; M. A. Gómez-Muñoz et al. 2023). The PN has also been classified in a catalog as having a bipolar core (L. Stanghellini & M. Haywood 2010). Although 3D kinematic modeling has led to the reclassification of certain elliptical PNe as bipolar (D. Jones et al. 2012), Hu 1-1 is accepted as elliptical. This morphology is interesting as molecule-rich PNe are typically bipolar or multipolar. There has also been some speculation that Hu 1-1 is a binary system (C. Muthu & B. G. Anandarao 1999), but this has not been confirmed. The nebula has an estimated evolutionary age of 6500 yr (G. Stasińska et al. 1997) and is located at a distance of 3.86 kpc (J. P. Phillips 2004). The central star has a temperature

Table 2
Target List of Planetary Nebulae

Source	α (J2000) (h m s)	δ (J2000) (deg arcmin arcsec)	θ_s[a] (arcsec)	Distance (kpc)	Age (yr)	Morphology	T_* (K)	Notes
M4-17	20:09:01.9	+43:43:43.5	30	2.2[b]	9,000[a]	Bipolar[c]	127,000[d]	H_2
Hu 1-1	00:28:15.4	+55:57:54.5	15	3.86[e]	6,500[f]	Elliptical[c]	113,500[d]	...
M1-59	18:43:20.2	−09:04:49.1	5	3.54[e]	4,050[g]	Multipolar[g]	117,500[h], 123,000[d]	H_2
Na 2	19:18:19.5	−11:06:16.2	18	9[i]	27,000[a]	Bipolar[j]	...	H_2

Notes.
[a] This work. Calculated age and assumed source size
[b] M. A. Guerrero et al. (2000).
[c] A. Manchado et al. (1996).
[d] L. Stanghellini et al. (2002).
[e] J. P. Phillips (2004).
[f] G. Stasińska et al. (1997).
[g] C.-H. Hsia et al. (2014).
[h] F. Palla et al. (2000).
[i] R. L. M. Corradi & H. E. Schwarz (1993).
[j] H. E. Schwarz et al. (1992).

of 113,500 K (L. Stanghellini et al. 2002), indicative of a high-excitation PN (N. Aksaker et al. 2015). Hu 1-1 is also a carbon-rich object, exhibiting a C/O ratio of ∼2.1–2.5 as determined from radio recombination lines (G. Delgado-Inglada & M. Rodriguez 2014; A. Peimbert et al. 2014). Based on the A. Manchado et al. (1996) image, and a comparison of 12 m and IRAM 30 m line intensities, we adopt a size of 15″ for this source.

The $J = 1 \rightarrow 0$ line of HCN and the $J = 2 \rightarrow 1$ line of CO previously observed in Hu 1-1 show an asymmetric line profile with a broad redshifted wing (P. J. Huggins et al. 2005; D. R. Schmidt et al. 2022); also see the improved line profile for HCN in Figure 3. D. R. Schmidt et al. (2022) additionally detected the $J = 3 \rightarrow 2$ line of HCN and a very weak HCO^+: $J = 1 \rightarrow 0$ transition toward Hu 1-1.

As shown in Figure 3, new detections of CN, CCH, HNC, CS, H_2CO, and c–C_3H_2 were made toward Hu 1-1. In addition, the existing data for HCN and HCO^+ in their $J = 1 \rightarrow 0$ transitions were improved, confirming the presence of HCO^+. HCN ($J = 3 \rightarrow 2$) was also improved. For CN, the two spin components of the $N = 2 \rightarrow 1$ transition were detected, indicated by lines under the spectra, and similarly for CCH in the $N = 2 \rightarrow 1$ (both 12 m and IRAM data) and $N = 3 \rightarrow 2$ transitions. Three lines of CS were identified ($J = 2 \rightarrow 1$, $J = 3 \rightarrow 2$, and $J = 5 \rightarrow 4$), three of H_2CO ($J_{Ka,Kc} = 2_{1,2} \rightarrow 1_{1,1}$, $J_{Ka,Kc} = 2_{0,2} \rightarrow 1_{0,1}$, and $J_{Ka,Kc} = 2_{1,1} \rightarrow 1_{1,0}$ (12 m and IRAM), and three of c–C_3H_2 ($J_{Ka,Kc} = 3_{1,2} \rightarrow 2_{2,1}$, $J_{Ka,Kc} = 4_{1,4} \rightarrow 3_{0,3}$, and $J_{Ka,Kc} = 3_{2,2} \rightarrow 2_{1,1}$). Finally, two transitions of HNC ($J = 1 \rightarrow 0$ and $J = 3 \rightarrow 2$) were successfully measured, as well as the $H^{13}CN$: $J = 2 \rightarrow 1$ line.

Line parameters for these spectra are provided in Table 4. The LSR velocities cluster around -62 km s^{-1} and the line widths are consistently near 25–30 km s^{-1}. Again, these values are in agreement with previous works. The line widths of CN and CCH are somewhat broader due to hyperfine structure. Most intensities are <10 mK, with the strongest features, ∼20 mK, arising from CN. The CO $J = 2 \rightarrow 1$ line was ∼75 mK, from D. R. Schmidt et al. (2022).

M1-59: This nebula is clearly multipolar (see Figure 1), speculated to contain three bipolar flows oriented in different directions, along with a central cavity or torus (C.-H. Hsia et al. 2014). The central source size is quoted as 4.″8 (J. P. Phillips & R. A. Márquez-Lugo 2011). M1-59 is estimated to be around 4050 yr old (C.-H. Hsia et al. 2014) and is located at a distance of 3.54 kpc (J. P. Phillips 2004). The temperature of the central star is reported as 117,500 K by F. Palla et al. (2000) and 123,000 K by L. Stanghellini et al. (2002). Previous observations of CO were conducted by G. T. Gussie & A. R. Taylor (1995), J. Sun & Y. Sun (2000), and P. J. Huggins et al. (2005). An absorption feature near -44 km s^{-1} was identified in the $J = 1 \rightarrow 0$ spectrum, attributed to galactic contamination, which is also observed in our data (see below). Huggins et al. described the $J = 2 \rightarrow 1$ line profile as a single component with tentative line wings. Recently, D. R. Schmidt et al. (2022) detected HCN ($J = 1 \rightarrow 0$ and $J = 3 \rightarrow 2$) and HCO^+ ($J = 3 \rightarrow 2$) toward M1-59. There was little evidence of line wings in these data, which included the $J = 2 \rightarrow 1$ line of CO. The spectra here do not exhibit line wings or multiple velocity components. In this work, a source size of 5″ was adopted based on its HST image, focusing on the central region.

In M1-59, the new molecular detections include CN, CCH, CS, HNC, and remarkably, H_2S, as well as $H^{13}CN$. The spectra are presented in Figure 4. In addition to HCO^+ ($J = 3 \rightarrow 2$), the $J = 1 \rightarrow 0$ transition of HCO^+ was also observed, partially blended with H(59)γ recombination line, confirming the original detection by D. R. Schmidt et al. (2022). The CO $J = 1 \rightarrow 0$ line was measured, and improved sensitivity was obtained for the previous HCN data of D. R. Schmidt et al. (2022). CN and CCH were identified on the basis of their spin–rotation components in the $N = 2 \rightarrow 1$ and $N = 3 \rightarrow 2$ transitions, respectively, indicated underneath the spectra. Two transitions of CS were detected ($J = 3 \rightarrow 2$ and $J = 5 \rightarrow 4$), and one line each for HNC ($J = 3 \rightarrow 2$), $H^{13}CN$ ($J = 2 \rightarrow 1$), and H_2S ($J_{Ka,Kc} = 1_{1,0} \rightarrow 1_{0,1}$). A recombination line from H(35)α is observed near the CS, $J = 3 \rightarrow 2$ spectrum. Galactic contamination near the CO, $J = 1 \rightarrow 0$ data to blueshifted velocities has been removed.

Table 5 summarizes the spectral analysis for M1-59. Typical line intensities are $\leqslant$ 10 mK. The LSR velocities observed are all near 109 km s^{-1}, with line widths about 20–25 km s^{-1}, excluding broadening due to hyperfine structure.

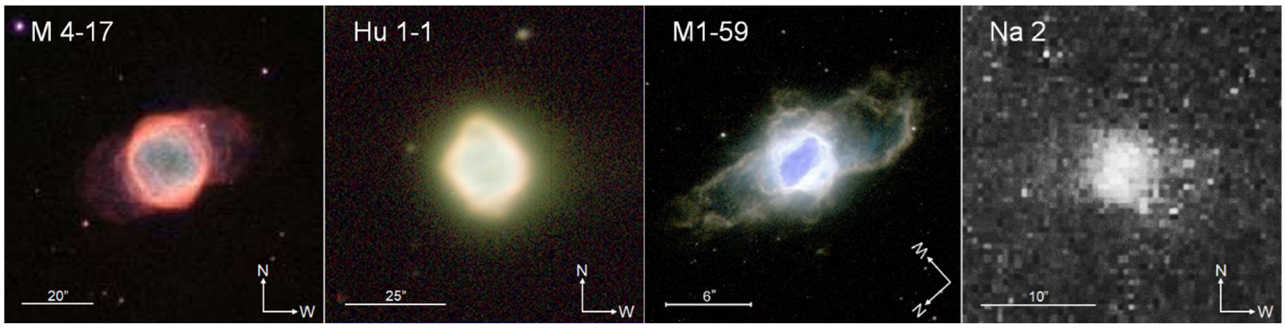

Figure 1. Images of the PNe studied in this work, M4-17, Hu 1-1, M1-59, and Na 2, from L. F. Miranda et al. (2010), A. Manchado et al. (1996), C.-H. Hsia et al. (2014), and J. H. Kastner et al. (1996). The first three are log-scale optical images in [N II] (red), Hα (green), and [O III] (blue). For Na 2, the 2.122 μm S(1) transition of H_2 is shown on a linear gray scale. Spatial scales are marked. North and west are shown for each source.

Na 2: This nebula displays a bipolar morphology, based on Hα, [O III], and [N II] images (H. E. Schwarz et al. 1992; R. L. M. Corradi & H. E. Schwarz 1993). The nebula is situated at a distance of 9 ± 1 kpc (R. L. M. Corradi & H. E. Schwarz 1993). Including the faint extensions of the lobes in [N II], Corradi & Schwarz estimated a source size near 40″. Both CO and H_2 have been observed in Na 2 (P. J. Huggins et al. 2005; J. H. Kastner et al. 1996). Huggins identified a double-peaked profile in the CO $J = 2 \rightarrow 1$ transition, while Kastner et al. concluded that the PN had an "hourglass" morphology. D. R. Schmidt et al. (2022) observed HCO^+ ($J = 1 \rightarrow 0$ and $J = 3 \rightarrow 2$) along with CO ($J = 1 \rightarrow 0$ and $J = 2 \rightarrow 1$) toward this PN. Given an expansion velocity of 19 km s^{-1} (based on the molecular line widths) and the quoted distance, the age of Na 2 is estimated to be around 27,000 yr, in agreement with the Schmidt et al. value of around 28,000 yr. Based on the H_2 2-micron image (J. H. Kastner et al. 1996), the source size used here is 18″.

As shown in Figure 5, CN and CCH were newly detected toward Na 2—striking results, given the calculated source age. For CN, the $N = 1 \rightarrow 0$ and $N = 2 \rightarrow 1$ lines were identified, the latter showing its distinct spin–rotation structure. The spin doublets of the $N = 3 \rightarrow 2$ transition of CCH were detected, but the intensity of the $J = 5/2 \rightarrow 3/2$ component is quite low; quantum-mechanically, this line is expected to be weaker. In addition, the spectra of HCO^+ ($J = 1 \rightarrow 0$ and $J = 3 \rightarrow 2$) and CO ($J = 1 \rightarrow 0$) have improved signal-to-noise ratios in comparison to the original D. R. Schmidt et al. (2022) data. These authors also reported the nondetection of HCN in Na 2. Despite the additional signal-averaging, HCN was still not detected, with 5σ upper limits of 1.3 mK ($J = 1 \rightarrow 0$) and 4 mK ($J = 3 \rightarrow 2$).

The line parameters for observed species are given in Table 6. All line intensities are <10 mK, including CO. The line widths are near 40 km s^{-1}, with little evidence of double-peaked profiles. The LSR velocities are near 110 km s^{-1}, consistent with $V_{\rm LSR} = 113 \pm 10$ km s^{-1} obtained by Corradi & Schwarz.

4. Analysis

The RADEX non-LTE radiative transfer code (F. F. S. van der Tak et al. 2007) was used to determine the column densities of the detected molecules. This one-dimensional model assumes an isothermal, homogeneous medium. RADEX calculates line intensities within the modeled medium using the Sobolev escape probability method to account for optical depth effects. Calculated intensities are compared to those observed to constrain the gas kinetic temperature, H_2 density, and molecular column density.

Typically, no more than two transitions were detected per molecule. Consequently, in the modeling, the kinetic temperature was held constant at $T_K = 20$ K, a common value for molecular gas in PNe (e.g., E. D. Tenenbaum et al. 2009; J. L. Edwards et al. 2014). However, in the case of Hu 1-1, three rotational transitions of CS were observed, permitting the kinetic temperature to be varied, with a best fit near 20 K. When only one transition of a given molecule was detected, the H_2 density was held constant, using values determined from other molecules with two or more observed transitions.

Given that the ortho ($K_a = 1, 3, 5, ...$) and para ($K_a = 0, 2, 4, ...$) states of H_2CO and c–C_3H_2 are distinguishable, in particular at the lower temperatures of PNe, they were treated separately. Two ortho transitions were observed in this work for each molecule, such that H_2 density and column density were varied in the RADEX calculations. For the para transition, the molecular column density was varied while the H_2 density was fixed to the value determined from the ortho transitions. The values given in Table 7 for H_2CO and c–C_3H_2 represent the sum of the ortho and para column densities.

In the analysis, molecular column densities were varied between $N_{\rm tot} \sim 10^{10}$ and 10^{15} cm^{-2} for all molecules except CO, where the range 10^{15} and 10^{18} cm^{-2} was applied. HCN, HCO^+, and CO column densities were re-evaluated on the basis of the new data obtained since the Level 2 paper (D. R. Schmidt et al. 2022). The updated values are consistent with those previously reported. The H_2 density was varied between 1×10^3 and 5×10^7 cm^{-3} in the analysis. Values found in the fitting typically fell in the range of 4.0×10^5 to 1.5×10^7 cm^{-3}, with somewhat lower densities for CO ($1.0–3.5 \times 10^4$ cm^{-3}). The column densities derived for all molecules other than CO were $N_{\rm tot} \sim 10^{11}$–10^{13} cm^{-2}. The resultant column densities and corresponding H_2 densities are listed in Table 7. Uncertainties in the column densities were based on the measured antenna temperatures.

To estimate fractional abundances, H_2 column densities are required. $N(H_2)$ of 1.6×10^{19} cm^{-2} was determined for M4-17 using H_2, $v = 1$-0 S(0) through S(3) flux values measured by R. A. Marquez-Lugo et al. (2015) and the method described in A. Youngblood et al. (2018). An excitation temperature of 1070 K was adopted for this source, based on a population

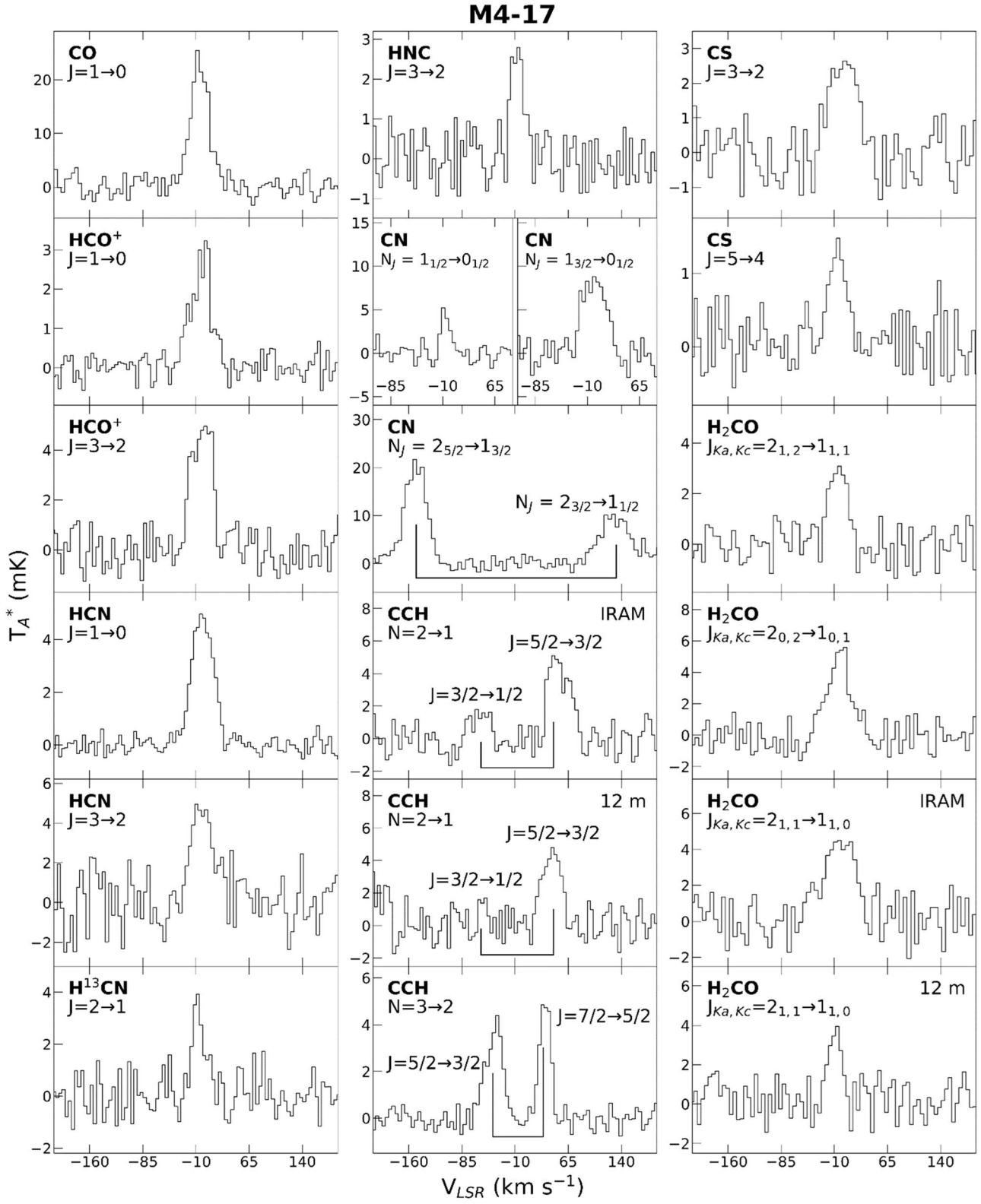

Figure 2. Spectra of molecular transitions observed toward the planetary nebula M4-17 obtained with the ARO telescopes (1, 2, and 3 mm) and the IRAM 30 m (2 mm); see Table 1. Among the new detections in this PN are HNC, CN, CCH, CS, and H_2CO, identified by the various transitions indicated. $H^{13}CN$ has also been observed, as shown. The $N = 2 \rightarrow 1$ line of CCH and the $J_{Ka,Kc} = 2_{1,1} \rightarrow 1_{1,0}$ line of H_2CO were observed at both the ARO 12 m and the IRAM 30 m, as indicated. The fine-structure splittings for CCH ($N = 2 \rightarrow 1$ and $N = 3 \rightarrow 2$) and CN ($N = 2 \rightarrow 1$) are shown underneath the spectra, except for the CN $N = 1 \rightarrow 0$ line, where separate spectra are displayed. Improved data are also shown for CO, HCN, and HCO^+ (see text). The spectra were observed with 0.3–0.5 km s^{-1} (IRAM), 1.1–1.8 km s^{-1} (12 m), and 1.1–1.3 km s^{-1} (SMT) resolution and smoothed to 4.5–6.5 km s^{-1}. The temperature scale is T_A^* (mK).

analysis of the H_2, $v = 1$–0 levels. Note that Marquez-Lugo et al. reported a much higher excitation temperature range of 2360–2520 K, including the $v = 2$ level.

For M1-59, H_2 measurements have been conducted for the $v = 1$–0, S(1) rovibrational line of H_2 at 2.122 μm from M. A. Guerrero et al. (2000). An excitation temperature

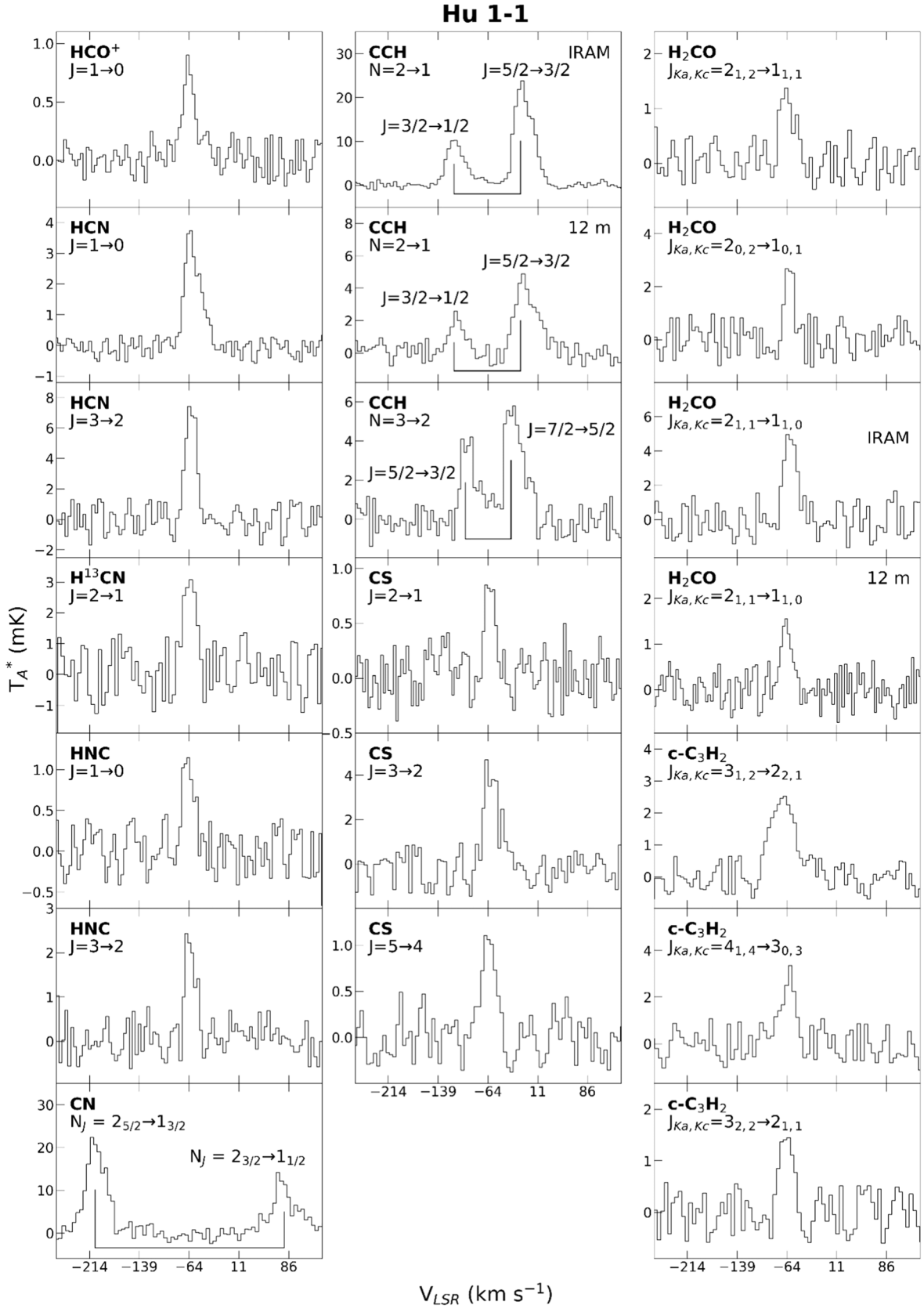

Figure 3. Spectra of molecular transitions observed toward the planetary nebula Hu 1-1 obtained with the ARO telescopes (1, 2, and 3 mm) and the IRAM 30 m (2 mm); see Table 1. New detections are HNC, CN, CCH, CS, H_2CO, and c–C_3H_2, identified by the transitions indicated. $H^{13}CN$ has also been observed, as shown. The $N = 2 \rightarrow 1$ line of CCH and the $J_{Ka,Kc} = 2_{1,1} \rightarrow 1_{1,0}$ line of H_2CO were observed at both the ARO 12 m and the IRAM 30 m, as indicated. The fine-structure splittings for CCH ($N = 2 \rightarrow 1$ and $N = 3 \rightarrow 2$) and CN ($N = 2 \rightarrow 1$) are shown underneath the spectra. Improved data are also shown for HCN and HCO^+ (see text). The spectra were observed with 0.3–0.5 km s^{-1} (IRAM), 1.1–1.8 km s^{-1} (12 m), and 1.1–1.3 km s^{-1} (SMT) resolution and have been smoothed to 4–6 km s^{-1}. The temperature scale is T_A^* (mK).

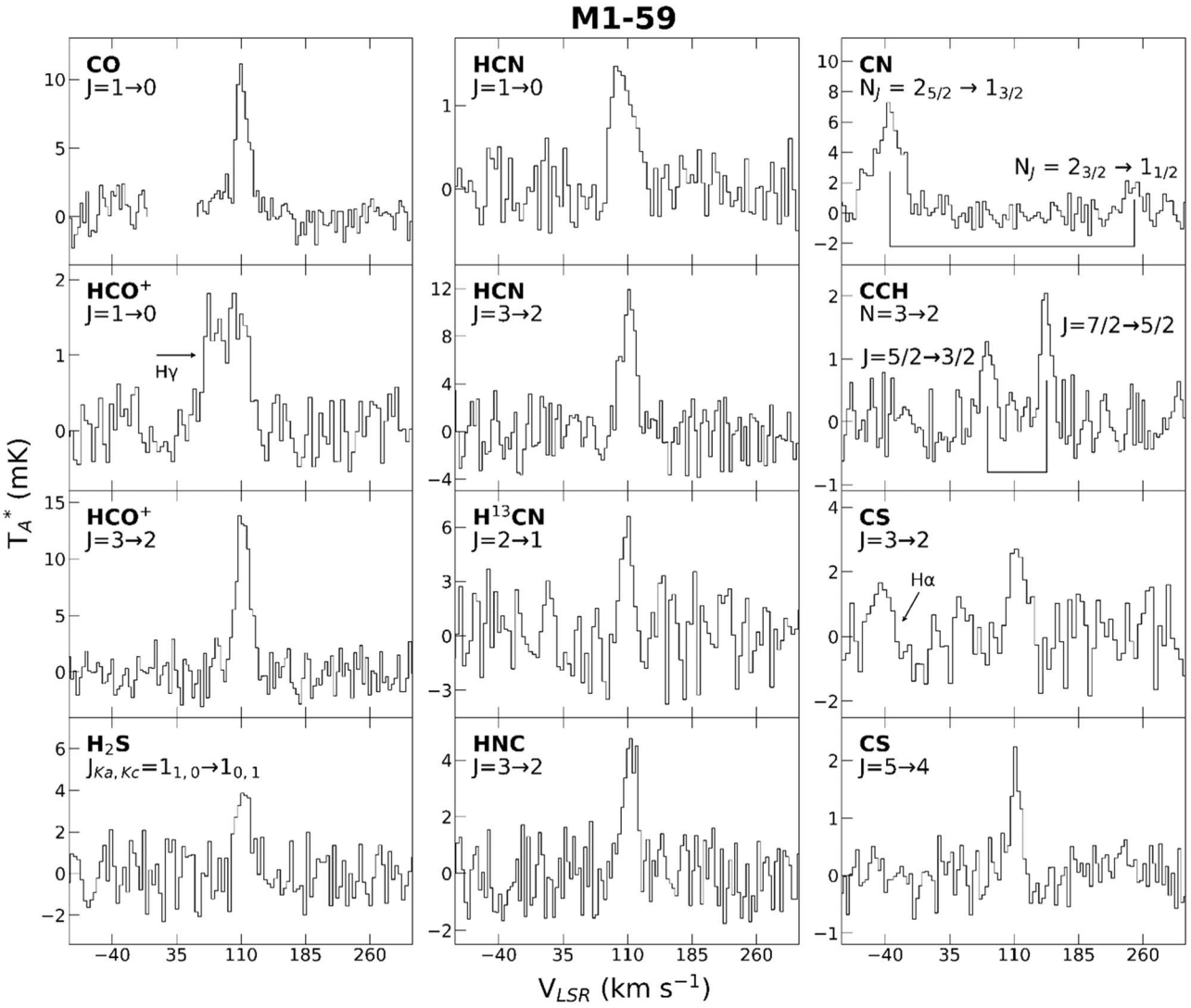

Figure 4. Spectra of molecular transitions observed toward the planetary nebula M1-59 obtained with the ARO telescopes (1, 2, and 3 mm) and the IRAM 30 m (2 mm); see Table 1. New detections in this PN are HNC, CN, CCH, and CS, identified by the transitions indicated, as well as $H^{13}CN$. Also presented (lower left corner) is the spectrum of the $J_{Ka,Kc} = 1_{1,0} \rightarrow 1_{0,1}$ transition of H_2S, a new molecule in PNe. The fine-structure splittings for CCH ($N = 3 \rightarrow 2$) and CN ($N = 2 \rightarrow 1$) are shown underneath the spectra. Improved data are also shown for CO, HCN, and HCO^+ (see text). Channels containing galactic contamination in the CO: $J = 1 \rightarrow 0$ panel are omitted. Hydrogen radio recombination lines appear in the HCO^+; $J = 1 \rightarrow 0$ and CS: $J = 3 \rightarrow 2$ panels, as indicated. The spectra were observed with 0.3–0.5 km s^{-1} (IRAM), 1.1–1.8 km s^{-1} (12 m) and 1.1–1.3 km s^{-1} (SMT) resolution and have been smoothed to 3–5 km s^{-1}. The temperature scale is T_A^* (mK).

of 1000 K was adopted, as is typical for PNe. The resultant H_2 column density was determined to be 2.3×10^{20} cm^{-2}.

No H_2 measurements are available for Hu 1-1, and only a very general estimate for Na 2. In this case, fractional abundances relative were approximated from CO, assuming $CO/H_2 \sim 10^{-4}$. This ratio is typical for PNe (e.g., A. P. Healy & P. J. Huggins 1990; P. J. Huggins et al. 2002; L. N. Zack & L. M. Ziurys 2013; J. L. Edwards et al. 2014). The calculated fractional abundances are reported in Table 7.

5. Discussion

5.1. Overview of Abundances: More Organic Molecules in PNe

These observations add to the inventory of PNe that have an active chemistry. Note that M4-17, Hu 1-1, and M1-59 have ages in the range 4050–9000 yr. They all have similar stellar temperatures (113,500–127,000 K) but different morphologies (bipolar, elliptical, and multipolar); see Table 2. Although bipolar in nature, Na 2 is much older and is in a class by itself. Beyond HCN and HCO^+, as studied by D. R. Schmidt et al. (2022), all four sources contain the free radicals CN and CCH. CN and CCH have previously been observed in other PNe, including the Helix and the Red Spider (E. D. Tenenbaum et al. 2009; J. L. Edwards & L. M. Ziurys 2013, 2014; D. R. Schmidt et al. 2018a). Abundances in this work were found in the ranges $f(CN/H_2) \sim 0.9–7.5 \times 10^{-7}$ and $f(CCH/H_2) \sim 0.8–7.5 \times 10^{-7}$, with the lowest values for Na 2. Column densities for these two molecules were the highest among those detected ($N_{tot} \sim 1–6 \times 10^{13}$ cm^{-2}, with 5×10^{12} cm^{-2} for Na 2), with the exception of CO. CS and HNC have been identified in M4-17, Hu 1-1, and M1-59, as well, with $N_{tot} \sim 0.7–9 \times 10^{12}$ cm^{-2} and $0.6–4 \times 10^{12}$ cm^{-2}, corresponding to $f(CS/H_2) \sim 1–5 \times 10^{-8}$ and $f(HNC/H_2) \sim 0.5–4 \times 10^{-8}$. Again, both molecules have been observed in other nebulae (see below and P. Cox et al. 1992; Y. Zhang et al. 2008; J. L. Edwards & L. M. Ziurys 2013, 2014; J. L. Edwards et al. 2014; D. R. Schmidt & L. M. Ziurys 2017a). The variation in abundances is therefore

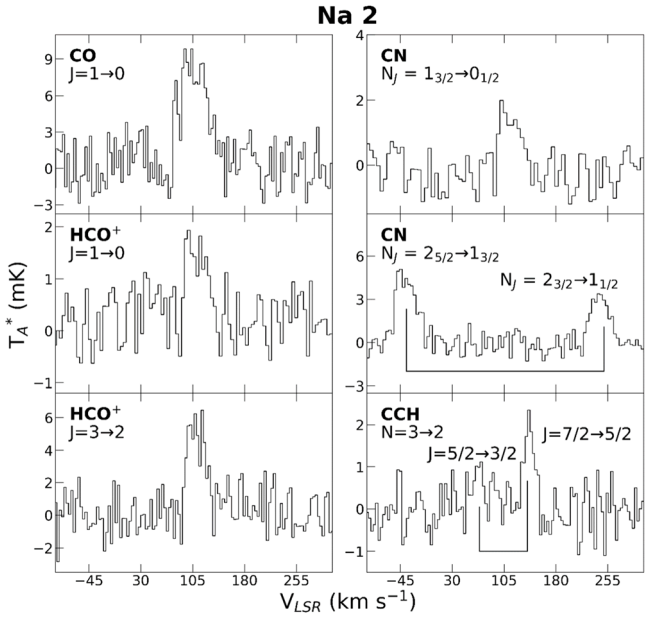

Figure 5. Spectra of molecular transitions observed toward the planetary nebula Na 2 obtained with the ARO telescopes (1 and 3 mm); see Table 1. The new detections are CN, observed in both the $N = 1 \rightarrow 0$ and $N = 2 \rightarrow 1$ transitions, and CCH, $N = 3 \rightarrow 2$. The fine-structure splittings for CCH ($N = 3 \rightarrow 2$) and CN ($N = 2 \rightarrow 1$) are shown underneath the spectra. One ($J = 5/2 \rightarrow 3/2$) spin component of CCH, which is quantum-mechanically expected to be weaker, has a low intensity. Improved data are also shown for CO and HCO^+ (see text). The spectra were observed with 1.1–1.8 km s^{-1} (12 m) and 1.1–1.3 km s^{-1} (SMT) resolution and have been smoothed to 3–5 km s^{-1}. The temperature scale is T_A^* (mK).

less than a factor of 10 among these four sources for CN, CCH, CS, and HNC. Also note that, for these PNe, the addition of new data has resulted in slightly revised HCN and HCO^+ abundances, with $f(HCN/H_2) \sim 1.4 \times 10^{-8}$–$1.1 \times 10^{-7}$ and $f(HCO^+/H_2) \sim 0.4$–4.1×10^{-8}.

H_2CO was detected in M4-17 and Hu 1-1, with abundances of 3.5×10^{-7} and 2.7×10^{-7}, respectively, with column densities near 6×10^{12} cm^{-2} (see Table 7). This work expands the list of PNe where H_2CO has been identified from three to five sources. H_2CO is seen in K4-47 ($f \sim 1.1 \times 10^{-7}$; D. R. Schmidt & L. M. Ziurys 2019), the Red Spider Nebula, NGC 6537 ($f \sim 2.2 \times 10^{-8}$; J. L. Edwards & L. M. Ziurys 2013), and the Helix Nebula, where the abundances vary from 2.5×10^{-8} to 2.1×10^{-7} across the source (L. N. Zack & L. M. Ziurys 2013).

T. Hasegawa et al. (2000) predicted an H_2CO abundance of $f \sim 10^{-12}$ for the wind component in their steady-state chemical model for the planetary nebula NGC 7027. However, observed values in these five PNe are several orders of magnitude higher. Hasegawa et al. suggested that the low abundance of H_2CO results from its rapid destruction through reactions with C^+, leading to HCO^+. H_2CO is a factor of 2–10 more abundant than HCO^+ in four of the five PNe where it has been observed. It is likely that C^+ has alternative reaction pathways other than through H_2CO.

The c-C_3H_2 molecule was detected in Hu 1-1 with an abundance of 1.1×10^{-8}, corresponding to a column density of 2.4×10^{12} cm^{-2}. This species has been observed in only three other PNe to date: K4-47 (1.5×10^{-7}; Schmidt & Ziurys. 2019), NGC 7027 (8.3×10^{-9}; Y. Zhang et al. 2008), and the Helix Nebula (0.4–7.9×10^{-8}; D. R. Schmidt et al. 2018a). Age therefore does not appear to be a factor in the destruction of this molecule.

Table 3
Line Parameters for Molecules Detected toward M4-17[a]

Molecule	Transition	T_A^* (mK)	V_{LSR} (km s^{-1})	$\Delta V_{1/2}$ (km s^{-1})
CO	$J = 1 \rightarrow 0$	24 ± 3	-7.3 ± 4.9	31.9 ± 4.9
HCN	$J = 1 \rightarrow 0$[b]	4.5 ± 0.5	0.0 ± 6.3	40.2 ± 6.3
	$J = 3 \rightarrow 2$	4 ± 2	-3.5 ± 6.8	36.7 ± 6.8
$H^{13}CN$	$J = 2 \rightarrow 1$	4.0 ± 1.5[c]	-7.8 ± 6.6	30.9 ± 6.6
HCO^+	$J = 1 \rightarrow 0$	3.0 ± 0.5	-7.0 ± 4.2	34.2 ± 4.2
	$J = 3 \rightarrow 2$	4.5 ± 1.0	-3.8 ± 4.5	38.1 ± 6.7
HNC	$J = 3 \rightarrow 2$	2.5 ± 1	-9.2 ± 6.6	26.4 ± 6.6
CN	$N_J = 1_{1/2} \rightarrow 0_{1/2}$[d]	4 ± 2	-9.1 ± 5.0	20.0 ± 5.0
	$N_J = 1_{3/2} \rightarrow 0_{1/2}$[b]	9 ± 3	~ -7	44.6 ± 5.0
	$N_J = 2_{3/2} \rightarrow 1_{1/2}$[b]	9 ± 2	-8.8 ± 5.3	42.3 ± 5.3
	$N_J = 2_{5/2} \rightarrow 1_{3/2}$[b]	20 ± 2	-4.9 ± 5.3	37.0 ± 5.3
CCH	$N_J = 2_{5/2} \rightarrow 1_{3/2}$[b]	5.0 ± 1.5[c]	-3.0 ± 4.7	42.2 ± 4.7
		4.0 ± 1.5	-5.7 ± 4.3	38.6 ± 4.3
	$N_J = 2_{3/2} \rightarrow 1_{1/2}$[b]	2.0 ± 1.5[c]	~ -5	~ 40
		~ 2	~ -4	~ 40
	$N_J = 3_{7/2} \rightarrow 2_{5/2}$[b]	4.5 ± 1.0	-3.9 ± 4.6	22.9 ± 6.9
	$N_J = 3_{5/2} \rightarrow 2_{3/2}$[b]	4.0 ± 1.0	-5.5 ± 4.6	32.0 ± 6.9
CS	$J = 3 \rightarrow 2$	~ 2[c]	~ -5	~ 35
	$J = 5 \rightarrow 4$	1.5 ± 0.5	-7.9 ± 4.9	34.3 ± 4.9
H_2CO	$J_{Ka,Kc} = 2_{1,2} \rightarrow 1_{1,1}$	3 ± 1	-3.3 ± 5.3	31.9 ± 5.3
	$J_{Ka,Kc} = 2_{0,2} \rightarrow 1_{0,1}$	5 ± 2[c]	-5.8 ± 5.2	37.4 ± 5.2
	$J_{Ka,Kc} = 2_{1,1} \rightarrow 1_{1,0}$	~ 4[c]	~ -5	~ 35
		4.0 ± 1.5	-11.8 ± 5.0	27.4 ± 5.0

Notes.
[a] Unless indicated, 2 and 3 mm lines measured with 12 m; 1 mm lines with SMT (see Table 1).
[b] Blend of hyperfine components
[c] Measured with the IRAM 30 m.
[d] Strongest hyperfine component.

Overall, CCH and CN are the most abundant species in this small sample of PNe, after CO and H_2. The prevalence of CCH is consistent with the findings of D. R. Schmidt & L. M. Ziurys (2017b), who noted that the abundance remains relatively constant across the AGB to PN transition, decreasing by only a factor of ~5. In other nebulae, such as NGC 6537, the CCH abundance is 6.9×10^{-8} (J. L. Edwards & L. M. Ziurys 2013), while the young PN NGC 7027 exhibits 5.4×10^{-8} (Y. Zhang et al. 2008). Old nebulae, such as K3–58 (~11,000 yr) and the Helix (~12,000 yr) also show high abundances of this molecule (2.4×10^{-6} and 1×10^{-6}, respectively; D. R. Schmidt & L. M. Ziurys 2017b). CCH is thought to form primarily through the photodissociation of HCCH during the late AGB and protoplanetary nebula (PPN) stages, with its abundance stabilizing as the PN phase begins. A. Ali et al. (2001) and D. A. Howe et al. (1994) estimate a fractional abundance of CCH in PNe near 3–5×10^{-7}, consistent with the observations. The Ali et al. prediction is only at 10,000 yr. M. P. Redman et al. (2003) predict an abundance three orders of magnitude lower ($f \sim 7 \times 10^{-10}$) at 10,050 yr. For CN, Howe et al. and Ali et al. predict $f \sim 10^{-6}$, independent of age—somewhat higher than observed—while Redman et al. calculate a drop from $\sim 10^{-6}$ to $\sim 10^{-9}$ from 2550 to 10,050 yr.

Both CCH and c-C_3H_2 could be possible precursors to C_{60} and C_{70}, the largest organic molecules known in PNe (e.g., see D. R. Schmidt & L. M. Ziurys 2017b). However, as far as can be discerned from the literature, there have been no attempts to search for C_{60} in the four PNe studied here. Furthermore, there have been no reported detections of the

Table 4
Line Parameters for Molecules Detected toward Hu 1-1[a]

Molecule	Transition	T_A^* (mK)	V_{LSR} (km s^{-1})	$\Delta V_{1/2}$ (km s^{-1})
HCN	$J = 1 \rightarrow 0$[b, c]	3.5 ± 0.5	-62.1 ± 4.2	29.6 ± 4.2
	$J = 3 \rightarrow 2$	7 ± 2	-63.3 ± 4.5	27.1 ± 4.5
$H^{13}CN$	$J = 2 \rightarrow 1$	2.5 ± 1.0[d]	-65.1 ± 5.1	30.5 ± 5.1
HCO^+	$J = 1 \rightarrow 0$	1.0 ± 0.3	-62.4 ± 6.3	22.9 ± 6.3
HNC	$J = 1 \rightarrow 0$	1.0 ± 0.5	-63.3 ± 6.2	24.8 ± 6.2
	$J = 3 \rightarrow 2$	2 ± 1	-64.4 ± 6.6	26.5 ± 6.6
CN	$N_J = 2_{3/2} \rightarrow 1_{1/2}$[c]	11 ± 2	-62.8 ± 5.3	37.0 ± 5.3
	$N_J = 2_{5/2} \rightarrow 1_{3/2}$[c]	20 ± 2	-60.0 ± 5.3	35.1 ± 5.3
CCH	$N_J = 2_{5/2} \rightarrow 1_{3/2}$[b, c]	22 ± 2[d]	-62.8 ± 5.0	40.2 ± 5.0
		4.5 ± 1.0	-62.5 ± 5.4	42.9 ± 5.4
	$N_J = 2_{3/2} \rightarrow 1_{1/2}$[b, c]	10 ± 2[d]	-64.7 ± 5.0	35.2 ± 5.0
		2.0 ± 1.0	-61.2 ± 5.4	34.8 ± 5.4
	$N_J = 3_{7/2} \rightarrow 2_{5/2}$[b, c]	5.0 ± 1.0	-61.6 ± 4.5	33.2 ± 4.5
	$N_J = 3_{5/2} \rightarrow 2_{3/2}$[b, c]	3.5 ± 1.0	-60.1 ± 6.8	25.9 ± 6.8
c-C_3H_2	$J_{Ka,Kc} = 3_{1,2} \rightarrow 2_{2,1}$	2 ± 1[d]	~ -62	~ 30
	$J_{Ka,Kc} = 4_{1,4} \rightarrow 3_{0,3}$	3 ± 1[d]	-64.5 ± 5.4	~ 30
	$J_{Ka,Kc} = 3_{2,2} \rightarrow 2_{1,1}$	1.5 ± 0.5[d]	-67.6 ± 5.3	31.6 ± 5.3
CS	$J = 2 \rightarrow 1$	0.8 ± 0.3	-62.7 ± 5.8	22.9 ± 5.8
	$J = 3 \rightarrow 2$[b,c]	4 ± 1	-62.0 ± 4.8	28.7 ± 4.8
	$J = 5 \rightarrow 4$	1.0 ± 0.5	-66.4 ± 4.9	29.4 ± 4.9
H_2CO	$J_{Ka,Kc} = 2_{1,2} \rightarrow 1_{1,1}$[b]	1.0 ± 0.5	-61.6 ± 5.3	31.9 ± 5.3
	$J_{Ka,Kc} = 2_{0,2} \rightarrow 1_{0,1}$	2.5 ± 1.0[d]	~ -63	~ 30
	$J_{Ka,Kc} = 2_{1,1} \rightarrow 1_{1,0}$	4.0 ± 1.5[d]	-62.5 ± 5.1	30.3 ± 5.1
		1.5 ± 0.5	-60.1 ± 5.1	25.3 ± 5.1

Notes.
[a] Unless indicated, 2 and 3 mm lines measured with 12 m; 1 mm lines with SMT (see Table 1).
[b] Redshifted line wing (see text).
[c] Blend of hyperfine components.
[d] Measured with the IRAM 30 m.

Table 5
Line Parameters for Molecules Detected toward M1-59[a]

Molecule	Transition	T_A^* (mK)	V_{LSR} (km s^{-1})	$\Delta V_{1/2}$ (km s^{-1})
CO	$J = 1 \rightarrow 0$	10 ± 2	109.8 ± 3.3	20.7 ± 3.3
HCN	$J = 1 \rightarrow 0$[b]	1.2 ± 0.5	106.3 ± 6.3	25.8 ± 6.3
	$J = 3 \rightarrow 2$	11 ± 3	109.4 ± 3.4	22.0 ± 3.4
$H^{13}CN$	$J = 2 \rightarrow 1$	6 ± 3[c]	107.1 ± 6.1	16.3 ± 6.1
HCO^+	$J = 1 \rightarrow 0$[d]	1.5 ± 0.5	107.6 ± 6.3	25.2 ± 6.3
	$J = 3 \rightarrow 2$	13 ± 3	110.6 ± 3.4	18.5 ± 3.4
HNC	$J = 3 \rightarrow 2$	4.5 ± 1.5	111.4 ± 3.3	19.8 ± 3.3
CN	$N_J = 2_{5/2} \rightarrow 1_{3/2}$[b]	6 ± 1	107.9 ± 4.0	37.7 ± 4.0
CCH	$N_J = 3_{7/2} \rightarrow 2_{5/2}$[b]	2.0 ± 0.5	108.2 ± 3.4	17.2 ± 3.4
	$N_J = 3_{5/2} \rightarrow ;2_{3/2}$[b]	1.0 ± 0.5	109.4 ± 5.2	20.2 ± 5.2
CS	$J = 3 \rightarrow 2$	2.5 ± 1.0[c]	111.7 ± 7.2	26.3 ± 7.2
	$J = 5 \rightarrow 4$	2.0 ± 0.5	110.1 ± 5.5	14.9 ± 5.5
H_2S	$J_{Ka,Kc} = 1_{1,0} \rightarrow 1_{0,1}$	4 ± 2[c]	111.0 ± 5.7	21.1 ± 5.7

Notes.
[a] Unless otherwise indicated, 2 and 3 mm lines measured with 12 m; 1 mm lines with SMT (see Table 1).
[b] Blend of hyperfine components.
[c] Measured with IRAM 30 m.
[d] Partial blend with H recombination line (see text).

Table 6
Line Parameters for Molecules Detected toward Na 2[a]

Molecule	Transition	T_A^* (mK)	V_{LSR} (km s^{-1})	$\Delta V_{1/2}$ (km s^{-1})
CO	$J = 1 \rightarrow 0$	9 ± 3	103.5 ± 4.9	40.1 ± 4.9
HCO^+	$J = 1 \rightarrow 0$	1.5 ± 0.5	110.9 ± 6.3	37.8 ± 6.3
	$J = 3 \rightarrow 2$	6 ± 2	108.9 ± 3.4	36.9 ± 3.4
CN	$N_J = 1_{3/2} \rightarrow 0_{1/2}$[b]	2 ± 1	110.2 ± 5.0	44.6 ± 5.0
	$N_J = 2_{3/2} \rightarrow 1_{1/2}$[b]	3 ± 1	103.9 ± 4.0	39.7 ± 4.0
	$N_J = 2_{5/2} \rightarrow 1_{3/2}$[b]	5 ± 2	106.3 ± 4.0	43.6 ± 4.0
CCH	$N_J = 3_{7/2} \rightarrow 2_{5/2}$[b]	1.5 ± 0.5	105.2 ± 6.9	27.5 ± 6.9
	$N_J = 3_{5/2} \rightarrow 2_{3/2}$[b]	~ 0.5	~ 105	~ 25

Notes.
[a] All 2 and 3 mm lines measured with 12 m; 1 mm lines with SMT (see Table 1).
[b] Blend of hyperfine components.

Unidentified Infrared Emission (UIE) bands in these objects, which are thought to arise from carbon compounds (e.g., S. Kwok 2022). In fact, there have been very limited IR observations in general of these nebulae. Outside of limited photometry measurements, only M1-59 has been studied spectroscopically; see K. Volk & M. Cohen (1990). Volk and Cohen reanalyzed low-resolution IRAS data in the 7–23 micron range and found only atomic transitions. C_{60} thus far has been detected in about a dozen galactic PNe (J. Cami et al. 2010; D. A. García-Hernández et al. 2010, 2012; C. Morisset et al. 2012; M. Otsuka et al. 2013, 2014) but none of these objects are known to contain CCH or c–C_3H_2. Based on these limited data, it is difficult to speculate whether these two molecules are involved in a "bottom-up" formation mechanism for C_{60} (e.g., Cherchneff 2006) or are degradation products of fullerenes (see D. R. Schmidt & L. M. Ziurys 2017b).

Table 7
Column Densities and Fractional Abundances

Source	Molecule	$n(H_2)$ (cm^{-3})	Column Density (cm^{-2})	$f(X/H_2)$
M4-17	CO[a]	2.2×10^4	$4.2 \pm 0.7 \times 10^{15}$	2.6×10^{-4}
	HCN	1.5×10^6	$1.7 \pm 0.3 \times 10^{12}$	1.1×10^{-7}
	$H^{13}CN$	1.5×10^6[b]	$2.9 \pm 0.9 \times 10^{11}$	2.8×10^{-8}
	HCO^+	4.5×10^5	$6.6 \pm 1.0 \times 10^{11}$	4.1×10^{-8}
	HNC	1.5×10^6[b]	$5.6 \pm 3.6 \times 10^{11}$	3.5×10^{-8}
	CN	4.5×10^6	$1.2 \pm 0.4 \times 10^{13}$	7.5×10^{-7}
	CCH	5.0×10^6	$1.2 \pm 0.5 \times 10^{13}$	7.5×10^{-7}
	CS	8.5×10^6	$7.2 \pm 1.7 \times 10^{11}$	4.5×10^{-8}
	H_2CO	2.5×10^4	$5.8 \pm 1.9 \times 10^{12}$[c]	3.5×10^{-7}
Hu 1-1	HCN	2.5×10^6	$2.9 \pm 0.4 \times 10^{12}$	1.4×10^{-8}
	$H^{13}CN$	2.5×10^6[b]	$1.4 \pm 0.3 \times 10^{11}$	6.7×10^{-10}
	HCO^+	2.5×10^6[b]	$7.5 \pm 3.0 \times 10^{11}$	3.6×10^{-9}
	HNC	1.0×10^6	$1.0 \pm 0.5 \times 10^{12}$	4.8×10^{-9}
	CN	4.0×10^5	$6.0 \pm 2.0 \times 10^{13}$	2.9×10^{-7}
	CCH	2.5×10^6	$2.6 \pm 0.9 \times 10^{13}$	1.2×10^{-7}
	$c\text{-}C_3H_2$	8.0×10^5	$2.4 \pm 0.8 \times 10^{12}$[d]	1.1×10^{-8}
	CS	1.0×10^6	$1.8 \pm 0.5 \times 10^{12}$	8.6×10^{-9}
	H_2CO	3.5×10^4	$5.5 \pm 1.9 \times 10^{12}$[e]	2.7×10^{-7}
M1-59	CO[a]	1.0×10^4	$2.3 \pm 0.5 \times 10^{16}$	1.0×10^{-4}
	HCN	1.0×10^7	$1.0 \pm 0.3 \times 10^{13}$	4.3×10^{-8}
	$H^{13}CN$	1.0×10^7[b]	$1.3 \pm 0.6 \times 10^{12}$	5.7×10^{-9}
	HCO^+	8.0×10^6	$6.0 \pm 1.3 \times 10^{12}$	2.6×10^{-8}
	HNC	1.0×10^7[b]	$3.7 \pm 1.2 \times 10^{12}$	1.6×10^{-8}
	CN	1.0×10^7[b]	$6.4 \pm 2.4 \times 10^{13}$	2.8×10^{-7}
	CCH	1.5×10^7	$3.5 \pm 1.9 \times 10^{13}$	1.5×10^{-7}
	CS	9.5×10^6	$9.0 \pm 1.1 \times 10^{12}$	3.9×10^{-8}
	H_2S	1.5×10^7[f]	$1.3 \pm 0.3 \times 10^{13}$	5.7×10^{-8}
Na 2	CO[a]	1.5×10^4	$5.6 \pm 0.5 \times 10^{15}$	1.0×10^{-4}[g]
	HCO^+	1.0×10^6	$6.5 \pm 2.2 \times 10^{11}$	1.2×10^{-8}
	CN	4.5×10^6	$5.0 \pm 1.6 \times 10^{12}$	8.9×10^{-8}
	CCH	7.5×10^6	$4.7 \pm 2.4 \times 10^{12}$	8.4×10^{-8}

Notes.
[a] Analysis included CO: $J = 2 \rightarrow 1$ data from D. R. Schmidt et al. (2022).
[b] Held constant with values from HCO^+ or HCN.
[c] Column density for ortho H_2CO was 4.0×10^{12} cm^{-2}, and for para H_2CO, 1.8×10^{12} cm^{-2}.
[d] Column density for ortho $c\text{-}C_3H_2$ was 1.8×10^{12} cm^{-2}, and for para $c\text{-}C_3H_2$, 2.3×10^{11} cm^{-2}.
[e] Column density for ortho H_2CO was 4.3×10^{12} cm^{-2}, and for para H_2CO, 1.2×10^{12} cm^{-2}.
[f] Held constant with value from CCH.
[g] Assumed value.

NGC 7027, in contrast, is a prominent carrier of the UIE bands and is a source of $c\text{–}C_3H_2$ (Y. Zhang et al. 2008). The other PNe with $c\text{–}C_3H_2$, the Helix, K4-47, and Hu1-1, are not known to contain the UIE, but there are very limited data for the latter two sources. There may be a connection between $c\text{–}C_3H_2$, CCH, and the UIE, but further studies are needed.

With our new detections, HNC has now been observed in over 20 PNe. In this study, HNC abundances were determined to be 3.5×10^{-8} for M4-17, 4.8×10^{-9} for Hu 1-1, and 1.6×10^{-8} for M1-59. High HNC abundances are found in both very young sources, such as K4-47 (1.4×10^{-7}), and very old sources, like the Helix (5×10^{-8}); see D. R. Schmidt & L. M. Ziurys (2017a). The HCN/HNC ratio has long been the subject of studies, with a more recent focus on PNe (D. R. Schmidt & L. M. Ziurys 2017a; J. Bublitz et al. 2019, 2022). In the nebulae studied here, the HCN/HNC ratios are remarkably consistent, with values near 3 for M4-17, Hu 1-1, and M1-59. Other PNe show ratios in the range ∼1–8 (J. L. Edwards & L. M. Ziurys 2013, 2014; D. R. Schmidt & L. M. Ziurys 2017a), aligning with the prediction of A. Ali et al. (2001) of HCN/HNC ∼ 2, based on a model of evolved PNe (>8000 yr old).

5.2. Sulfur-containing Molecules: Adding H_2S to the PN Inventory

The detection of H_2S in M1-59, identified via its $J_{Ka,Kc} = 1_{1,0} \rightarrow 1_{0,1}$ transition, is the first observation of this molecule in a PN. In M1-59, the abundance of H_2S is 5.7×10^{-8}, with N_{tot} of 1.3×10^{13} cm^{-2}. CS, in contrast, has a somewhat lower value of $f \sim 4 \times 10^{-8}$; Hu1-1 and M4-17 exhibit $f \sim 0.9 \times 10^{-8}$ and 5×10^{-8}. CS has been observed in five other PNe: K4-47, M2-48, NGC 6537 (Red Spider), NGC 6720 (Ring), and NGC 6853 (Dumbbell) (J. L. Edwards & L. M. Ziurys 2013; J. L. Edwards et al. 2014), with abundances of $f \sim 1\text{–}4 \times 10^{-8}$—consistent with the new observations. H_2S has also very recently been detected toward NGC 6537 and M2-48 (L. M. Ziurys & D. R. Schmidt 2024). Other sulfur-bearing molecules observed in PNe are SO (NGC 6537 and M2-48) and SO_2 (M2-48). An unsuccessful search was conducted toward M1-59 for SO (∼3–4 mK peak-to-peak noise level), but not SO_2. No models predict abundances for H_2S, with the exception of that of T. Hasegawa et al. (2000). They calculate $f \sim 3.5 \times 10^{-14}$ in their wind model—significantly lower than observed.

It is notable that the CS abundances in PNe ($f \sim 10^{-8}$) are generally lower than those of AGB stars, which have $f \sim 10^{-6}$ for C-rich circumstellar envelopes and 10^{-7}–10^{-6} in oxygen-rich environments (Y. Zhang et al. 2009; L. M. Ziurys et al. 2009, and references therein). The decrease in CS abundance from AGB stars to PNe suggests photodestruction in the PPN phase. Modeling of the CS abundance in PNe suggest $f \sim 10^{-8}$ near 10,000 yr, in reasonable agreement with the observations (M. P. Redman et al. 2003; A. Ali et al. 2001). H_2S, in contrast, is mainly in O-rich envelopes (T. Danilovich et al. 2017), including IK Tau, NML Cyg, and VY CMa (A. Omont et al. 1993; E. D. Tenenbaum et al. 2010; A. P. Singh et al. 2021). It has also been observed in IRC +10216 (J. Cernicharo et al. 1987, 2000). Typical circumstellar abundances for H_2S are 1×10^{-5} to 5×10^{-6} (A. Omont et al. 1993; A. P. Singh et al. 2021).

The presence of H_2S and CS in PNe could help resolve the so-called "sulfur anomaly," an observed deficit of this element in these objects (R. B. C. Henry et al. 2004). Sulfur abundances in planetary nebulae are expected to remain unmodified from their levels in the ISM at the time the progenitor star formed. However, R. B. C. Henry et al. (2004) found lower S abundances in a study of 85 PNe, relative to H II regions of the same metallicity. They attributed this deficit to the employed ionization correction factor, which may not have fully accounted for excess S^{3+} compared to model predictions. Yet the sulfur anomaly has been confirmed by subsequent studies, including those by J. Bernard-Salas (2006), S. R. Pottasch & J. Bernard-Salas (2006), R. A. Shaw et al. (2010), Kwitter & Henry (2012), and J. M. Green et al. (2011), with no clear consensus to its cause.

One potential explanation for the anomaly is that sulfur may be sequestered in dust or molecules, as suggested by R. B. C. Henry et al. (2012). As a hydride, H_2S is a likely sink for sulfur, although CS, SO, and SO_2 may be important carriers. S. Tan & Q. A. Parker (2024) recently suggested that the sulfur deficit is nearly absent in PNe with younger, higher-mass progenitors, but

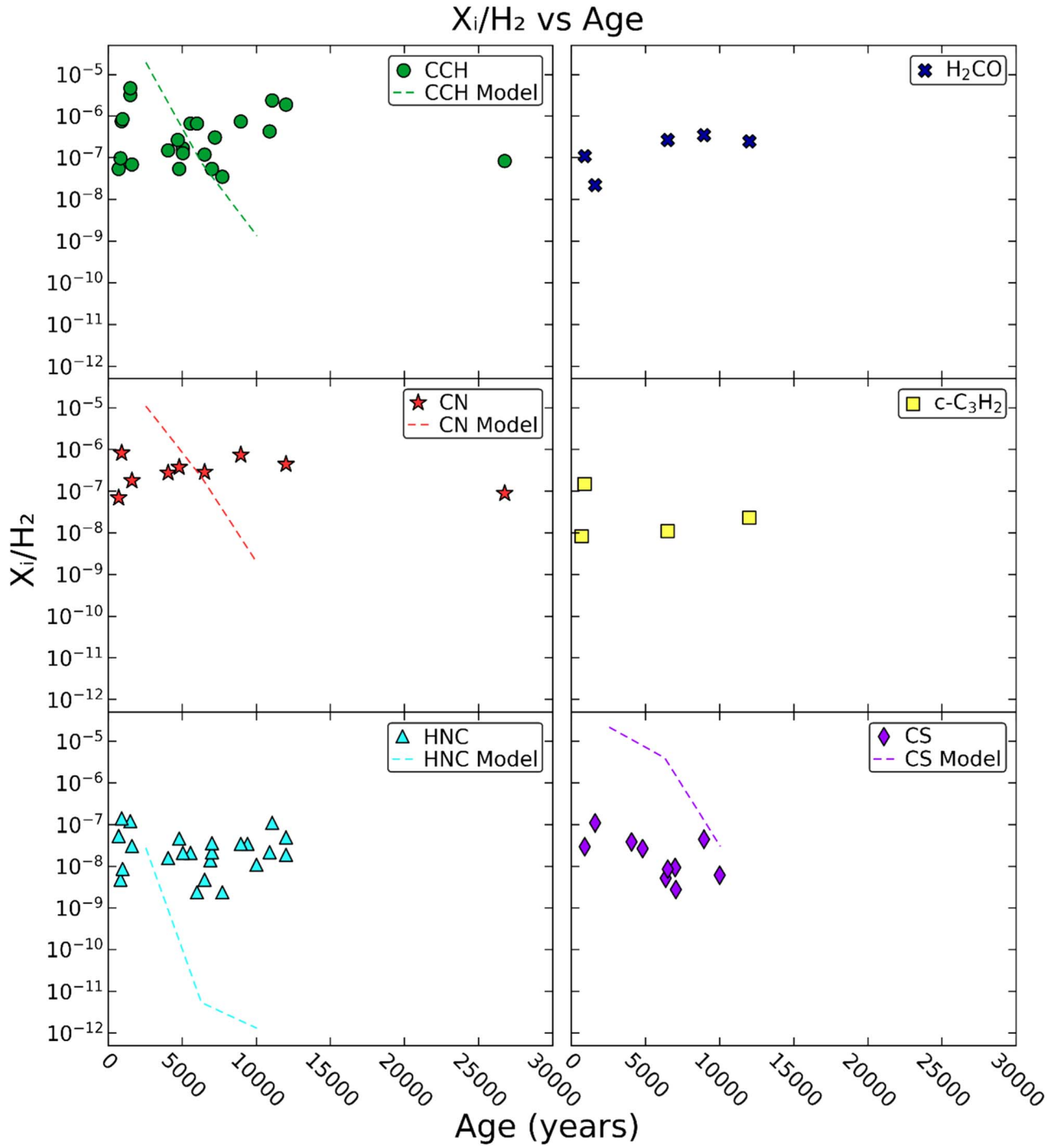

Figure 6. Plots of observed fractional abundances from this work and the literature (P. Cox et al. 1992; R. Bachiller et al. 1997; J. L. Edwards & L. M. Ziurys 2013, 2014; J. L. Edwards et al. 2014; D. R. Schmidt & L. M. Ziurys 2016, 2017a, 2017b, 2019; D. R. Schmidt et al. 2018a, 2018b, 2022) vs. ages of PNe (in year). Left column shows plots for CCH (green circles), CN (red stars), and HNC (teal triangles). Right column displays data for H_2CO (navy crosses), c–C_3H_2 (yellow squares), and CS (purple diamonds). Predictions from the M. P. Redman et al. (2003) model are also shown for CCH, CN, HNC, and CS by dashed lines. As these plots illustrate, observed abundances remain constant across the >12,000–25,000 yr PN lifespan for all six molecules, within factors of 10–60. In contrast, the model predicts decreases in abundance of three to four orders of magnitude, up to ∼10,000 yr.

is found in carbon-rich PNe with intermediate-mass stars. Unfortunately, our sample of planetary nebulae are not among the known deficient sources.

5.3. Molecular Abundances with Nebula Age: Further Data

J. L. Edwards et al. (2014), D. R. Schmidt & L. M. Ziurys (2016, 2017a, 2017b), D. R. Schmidt et al. (2018a, 2018b), Schmidt & Ziurys (2019), and D. R. Schmidt et al. (2022) found that abundances of HCN, HCO^+, CS, CCH, and HNC did not significantly vary with age across nearly 30,000 yr. This work expands this finding to new species: CN, H_2CO, and c–C_3H_2, and provides new data for CS, CCH, and HNC. Plots of observed fractional abundances of these six molecules versus the age of the PNe are shown in multiple panels in Figure 6. These data include this work and other values in the

literature, indicated in the caption. The left column shows the relationship for CCH (green circles), CN (red stars), and HNC (teal triangles); the right column displays data for H_2CO (navy crosses), c–C_3H_2 (yellow squares), and CS (purple diamonds). Predictions from the M. P. Redman et al. (2003) model at 2550, 6300, and 10,050 yr are also indicated for CCH, CN, HNC, and CS by dashed lines. As these plots illustrate, observed abundances remain relatively constant for all six molecules across the 12,000 or even ∼25,000 yr PN lifespan.

The abundances of CCH remain in the range 4×10^{-8}–5×10^{-6} with no downward trend out to 27,000 yr, just scatter within these values. A similar situation exists for CN, with $f \sim 7 \times 10^{-8}$–8×10^{-7}, again out to 27,000 yr. The new plots for HNC and CS improve on the previous diagrams of D. R. Schmidt & L. M. Ziurys (2017a) and J. L. Edwards et al. (2014), showing $f \sim 2 \times 10^{-9}$–1×10^{-7} to ∼10,000 yr. In all four cases, the models predict a decrease in abundance of 1000–10,000 up to ∼10,000 yr. This dramatic drop is not observed. Note that the model shows a high CS abundance of $\sim 10^{-5}$ near 2000 yr, which is also not observed. This result lends further credence to the idea that most chemical changes from the AGB phase occur in PPNe, with "freeze-out" in the PN stage (see D. R. Schmidt & L. M. Ziurys 2017a). Observations of the Helix Nebula have also shown that gas-phase molecules and dust are mixed in the dense clumps. Therefore, gas-phase molecules may condense onto grains at the typical clump temperatures of 20–30 K, and then are liberated at the clump edges from impinging UV radiation. The overall process must be steady-state because abundances do not change significantly with time. Note that chemical synthesis in PNe is quite different from that in molecular clouds. The timescales are much shorter (∼10,000–30,000 yr versus 10^6–10^7 yr), and there is more UV radiation and clumping of material.

There are fewer data points for H_2CO and c–C_3H_2, and no temporal model predictions. These molecules appear to hold near constant abundances in the range $f \sim 10^{-8}$–10^{-7}, up to 10,000 yr. Both species are widely observed across the Helix Nebula (L. N. Zack & L. M. Ziurys 2013; D. R. Schmidt et al. 2018a). More data on these complex "organics" are clearly needed.

Na 2, a very old planetary nebula, offers a rare glimpse into the chemistry in the very late PN stage. The presence of HCO^+, CN, and CCH in this source is striking, suggesting that the dense dust clumps that preserve the molecules from UV radiation from the central star are long-lived. E. D. Tenenbaum et al. (2009) calculated that a clump with $n \sim 3 \times 10^5$ cm^{-3} will dissipate in 10^7 yr into diffuse material with $A_v = 1$. In this time frame, the clump will travel ∼150 pc, assuming $V_{exp} = 15$ km s^{-1}, moving well away from its parent star. The detection of these radicals and ions in Na 2 is consistent with this scenario. Models such as that of Redman et al. start with clumps with densities $\sim 10^5$ cm^{-3}—about a factor of 10–100 more diffuse than observed. Perhaps increasing the clump density would improve model predictions.

5.4. Morphology and Molecular Content

M4-17 and Na 2 are bipolar nebulae, and M1-59 is quadrupolar. All three PNe contain polyatomic molecules such as HCO^+ and CCH. Na 2 is less chemically diverse, likely because of its age. M4-17 and M1-59 also contain HCN and HNC, and in the former source, H_2CO as well. It has been postulated that dense equatorial regions in bipolar PNe provide refuge for molecules from photodissociation and therefore foster H_2 (M. A. Guerrero et al. 2000; R. A. Marquez-Lugo et al. 2013). Indeed, most molecule-rich nebulae seem to be bipolar or multipolar in shape (P. J. Huggins et al. 1996, 2005; J. H. Kastner et al. 1996; D. R. Schmidt & L. M. Ziurys 2016, 2017a, 2017b; D. R. Schmidt et al. 2022). On the other hand, sensitive observations reveal that H_2 emission is typical in bipolar nebulae but not exclusive to them (R. A. Marquez-Lugo et al. 2013, 2015). Furthermore, high spatial resolution studies, such as that by R. A. Marquez-Lugo et al. (2013), have shown that the bright H_2 emission originates from dense knots or clumps of dust embedded in ionized gas. The dense knots, rather than torus-like structures, shield the molecules from photodissociation regions (P. Cox et al. 1998; A. K. Speck et al. 2002; A. Speck et al. 2003; M. Matsuura et al. 2009; R. A. Marquez-Lugo et al. 2013; A. Manchado et al. 2015).

Of the source sample, Hu 1-1 is quite chemically diverse, hosting the polyatomic species HCN, HCO^+, H_2CO, CCH, HNC, and c–C_3H_2. It is one of four PNe known to contain c–C_3H_2. Hu1-1 is classified as elliptical. This result suggests that chemical complexity is not necessarily tied to bipolar/multipolar morphology. Instead, other factors, such as central star temperature, may have a stronger influence on PN chemistry. Furthermore, the identification of CCH and c–C_3H_2 in Hu 1-1 demonstrates that the nebula is carbon-rich. O-rich PNe such as M2-48 have been shown to be devoid of CCH, despite intensive searches (J. L. Edwards & L. M. Ziurys 2014). In addition, the other three nebulae containing c–C_3H_2, K4-47, NGC 7027, and the Helix, are thought to have C > O (Y. Zhang et al. 2008; E. D. Tenenbaum et al. 2009; D. R. Schmidt et al. 2018a). It has been postulated that bipolarity in PNe is characteristic of C-rich objects (F. Stribling & A. Speck 2024). Thus, Hu 1-1, with its elliptical morphology and rich carbon chemistry may be an exception. Further molecular studies of elliptical and circular PNe need to be conducted to test the boundaries of these parameters.

Hu 1-1 also exhibits a higher $^{12}C/^{13}C$ ratio than M1-59 and M4-17, based on column densities of HCN and $H^{13}CN$. Although clearly preliminary, the ratios found are 5.9 ± 2.1 for M4-17, 20.7 ± 5.3 for Hu 1-1, and 7.7 ± 4.2 for M1-59. L. M. Ziurys et al. (2020) found that ratios for several C-rich bipolar nebulae, derived from multiple molecules, were surprisingly low, lying in the range $^{12}C/^{13}C \sim 1.0 \pm 0.7$–$13.2 \pm 4.9$, with an average value of 3.7. These ratios are significantly less than those found in the envelopes of C-rich AGB stars, and in some cases, the CNO equilibrium value of 3.5. The ratios measured in M4-17 and M1-59 are consistent with the Ziurys et al. findings. The value in Hu 1-1 is noticeably higher and more in line with ratios obtained in C-rich AGB stars (see L. M. Ziurys et al. 2020). Ziurys et al. speculated that the low $^{12}C/^{13}C$ ratios in PNe of bipolar/multipolar morphologies arose from an explosive process involving proton capture that occurred at the AGB–PN transition. Such a process would account for the enhancement of ^{13}C and the disruption of the spherical AGB shell. Hu 1-1, with its elliptical morphology, may have not undergone such an explosive process.

6. Conclusions

In the D. R. Schmidt et al. (2022) Level 2 PNe survey, HCN and HCO^+ were detected in M4-17, Hu 1-1, and M1-59, and the latter molecule in Na 2. This study has shown that all four nebulae contain other molecules, and even species as complex as H_2CO and c–C_3H_2. The inventory of chemically diverse planetary nebulae has therefore been expanded. Of particular note is the identification of CCH and CN in the very old PN Na 2, demonstrating that molecules can still be detected in the very late phases of PN evolution, albeit free radicals and ions. Also striking

is the presence of four- and five-atom molecules, H_2CO and c–C_3H_2, in Hu 1-1, thought to have elliptical morphology. Chemically rich PNe tend to be bipolar or multipolar in nature. Both CCH and c–C_3H_2 may be related to C_{60} or even the UIE, but additional studies are needed in the infrared of the PNe containing these molecules. Further molecular searches are clearly necessary to evaluate the chemistry in PNe and the connection between large and small molecules. Overall, there is growing evidence that PNe are significant contributors of molecular material to the diffuse ISM, seeding it with complex species that lay the foundation for chemical evolution in dense molecular clouds.

Acknowledgments

This research was supported by NSF grants AST-1907910 and AST-2307305.

ORCID iDs

K. R. Gold https://orcid.org/0000-0002-6830-6239
D. R. Schmidt https://orcid.org/0000-0001-7519-6819
L. M. Ziurys https://orcid.org/0000-0002-1805-3886

References

Aksaker, N., Yerli, S. K., Kızıloğlu, Ü., & Atalay, B. 2015, PASA, 32, 3
Ali, A., Shalabiea, O. M., El-Nawawy, M. S., & Millar, T. J. 2001, MNRAS, 325, 881
Bachiller, R., Forveille, T., Huggins, P. J., & Cox, P. 1997, A&A, 324, 1123
Balick, B., & Frank, A. 2002, ARA&A, 40, 439
Bernard-Salas, J. 2006, in IAU Symp. 234, Planetary Nebulae in our Galaxy and Beyond, ed. M. J. Barlow & R. H. Mendez (Cambridge: Cambridge Univ. Press), 181
Bublitz, J., Kastner, J. H., Hily-Blant, P., et al. 2022, A&A, 659, A197
Bublitz, J., Kastner, J. H., Standander-García, M., et al. 2019, A&A, 625, A101
Cami, J., Bernard-Salas, J., Peeters, E., & Malek, S. E. 2010, Sci, 329, 1180
Cernicharo, J., Guélin, M., Hein, H., & Kahane, C. 1987, A&A, 181, L9
Cernicharo, J., Guélin, M., & Kahane, C. 2000, A&AS, 142, 181
Cherchneff, I. 2006, A&A, 456, 1001
Corradi, R. L. M., & Schwarz, H. E. 1993, A&A, 278, 247
Cox, P., Boulanger, F., Huggins, P. J., et al. 1998, ApJ, 495, L23
Cox, P., Omont, A., Huggins, P. J., Bachiller, R., & Forveille, T. 1992, A&A, 266, 420
Danilovich, T., Van de Sande, M., De Beck, E., et al. 2017, A&A, 606, A124
Delgado-Inglada, G., & Rodríguez, M. 2014, ApJ, 784, 173
Edwards, J. L., Cox, E. G., & Ziurys, L. M. 2014, ApJ, 791, 79
Edwards, J. L., & Ziurys, L. M. 2013, ApJL, 770, L5
Edwards, J. L., & Ziurys, L. M. 2014, ApJL, 794, L27
García-Hernández, D. A., Iglesias-Groth, S., Acosta-Pulido, J. A., et al. 2011, ApJL, 737, L30
García-Hernández, D. A., Manchado, A., García-Lario, P., et al. 2010, ApJL, 724, L39
García-Hernández, D. A., Villaver, E., García-Lario, P., et al. 2012, ApJ, 760, 107
Gómez-Muñoz, M. A., Bianchi, L., & Manchado, A. 2023, ApJS, 226, 34
Green, J. M., Braxton, K., Balick, B., & Lutz, J. 2011, AAS Meeting, 217, 256.06
Guerrero, M. A., Villaver, E., Manchado, A., Garcia-Lario, P., & Prada, F. 2000, ApJS, 127, 125
Gussie, G. T., & Taylor, A. R. 1995, MNRAS, 273, 801
Hasegawa, T., Volk, K., & Kwok, S. 2000, ApJ, 532, 994
Healy, A. P., & Huggins, P. J. 1990, AJ, 100, 511
Henry, R. B. C., Kwitter, K. B., & Balick, B. 2004, AJ, 127, 2284
Henry, R. B. C., Speck, A., Karakas, A. I., Ferland, G. J., & Maguire, M. 2012, ApJ, 749, 61
Howe, D. A., Hartquist, T. W., & Williams, D. A. 1994, MNRAS, 271, 811
Hsia, C.-H., Chau, W., Zhang, Y., & Kwok, S. 2014, ApJ, 787, 25
Huggins, P. J., Bachiller, R., Cox, P., & Forveille, T. 1996, A&A, 315, 284
Huggins, P. J., Bachiller, R., Planesas, P., Forveille, T., & Cox, P. 2005, ApJS, 160, 272
Huggins, P. J., Forveille, T., Bachiller, R., et al. 2002, ApJL, 573, L55
Huggins, P. J., & Healy, A. P. 1989, ApJ, 346, 201
Iben, I., & Renzini, A. 1983, ARA&A, 21, 271
Jones, D., Mitchell, D. L., Lloyd, M., et al. 2012, MNRAS, 420, 2271
Kastner, J. H., Weintraub, D. A., Gately, I., Merrill, K. M., & Probst, R. G. 1996, ApJ, 462, 777
Kimura, R. K., Gruenwald, R., & Aleman, I. 2012, A&A, 541, A112
Kwitter, K. B., & Henry, R. B. C. 2012, in IAU Symp. 283, Planetary Nebulae: An Eye to the Future, ed. A. Manchado, L. Stanghellini, & D. Schönberner (Cambridge: Cambridge Univ. Press), 119
Kwok, S. 2022, Ap&SS, 367, 16
Manchado, A., Guerrero, M. A., Stanghellini, L., & Serra-Ricart, M. 1996 The IAC Morphological Catalog of Northern Galactic Planetary Nebulae (La Laguna: IAC)
Manchado, A., Stanghellini, L., Villaver, E., et al. 2015, ApJ, 808, 115
Marquez-Lugo, R. A., Guerrero, M. A., Ramos-Larios, G., & Miranda, L. F. 2015, MNRAS, 453, 1888
Marquez-Lugo, R. A., Ramos-Larios, G., Guerrero, M. A., & Vázquez, R. 2013, MNRAS, 429, 973
Matsuura, M., Speck, A. K., McHunu, B. M., et al. 2009, ApJ, 700, 1067
Miranda, L. F., Ramos-Larios, G., & Guerrero, M. A. 2010, PASA, 27, 180
Morisset, C., Szczerba, R., García-Hernández, D. A., & García-Lario, P. 2012, in IAU Symp. 283, Planetary Nebulae: An Eye to the Future, ed. A. Manchado, L. Stanghellini, & D. Schönberner (Cambridge: Cambridge Univ. Press), 452
Muthu, C., & Anandarao, B. G. 1999, BASI, 27, 171
Omont, A., Lucas, R., Morris, M., & Guilloteau, S. 1993, A&A, 267, 490
Otsuka, M., Kemper, F., Cami, J., Peeters, E., & Bernard-Salas, J. 2014, MNRAS, 437, 2577
Otsuka, M., Kemper, F., Hyung, S., et al. 2013, ApJ, 764, 77
Palla, F., Bachiller, R., Stanghellini, L., Tosi, M., & Galli, D. 2000, A&A, 355, 69
Peimbert, A., Peimbert, M., Delgado-Inglada, G., García-Rojas, J., & Peña, M. 2014, RMxAA, 50, 329
Phillips, J. P. 2004, MNRAS, 353, 589
Phillips, J. P., & Márquez-Lugo, R. A. 2011, RMxAA, 47, 83
Pottasch, S. R., & Bernard-Salas, J. 2006, A&A, 457, 189
Redman, M. P., Viti, S., Cau, P., & Williams, D. A. 2003, MNRAS, 345, 1291
Schmidt, D. R., Gold, K. R., Sinclair, A., Bergstrom, S., & Ziurys, L. M. 2022, ApJ, 927, 46
Schmidt, D. R., Woolf, N. J., Zega, T. J., & Ziurys, L. M. 2018b, Natur, 564, 378
Schmidt, D. R., Zack, L. N., & Ziurys, L. M. 2018a, ApJL, 864, L31
Schmidt, D. R., & Ziurys, L. M. 2016, ApJ, 817, 175
Schmidt, D. R., & Ziurys, L. M. 2017a, ApJ, 835, 79
Schmidt, D. R., & Ziurys, L. M. 2017b, ApJ, 850, 123
Schmidt, D. R., & Ziurys, L. M. 2019, ApJL, 881, L38
Schwarz, H. E., Corradi, R. L. M., & Melnick, J. 1992, A&AS, 96, 23
Shaw, R. A., Lee, T.-H., Stanghellini, L., et al. 2010, ApJ, 717, 562
Singh, A. P., Edwards, J. L., Humphreys, R. M., & Ziurys, L. M. 2021, ApJL, 920, L38
Speck, A. K., Meixner, M., Fong, D., et al. 2002, AJ, 123, 346
Speck, A. K., Meixner, M., Jacoby, G. H., & Knezek, P. M. 2003, PASP, 115, 170
Stanghellini, L., & Haywood, M. 2010, ApJ, 714, 1096
Stanghellini, L., Villaver, E., Manchado, A., & Guerrero, M. A. 2002, ApJ, 576, 285
Stasińska, G., Górny, S. K., & Tylenda, R. 1997, A&A, 327, 736
Stribling, F., & Speck, A. 2024, AAS Meeting, 243, 113.02
Sun, J., & Sun, Y. 2000, ScChA, 43, 217
Tan, S., & Parker, Q. A. 2024, ApJL, 961, L47
Tenenbaum, E. D., Dodd, J. L., Milam, S. N., Woolf, N. J., & Ziurys, L. M. 2010, ApJS, 190, 348
Tenenbaum, E. D., Milam, S. N., Woolf, N. J., & Ziurys, L. M. 2009, ApJ, 704, L108
van der Tak, F. F. S., Black, J. H., Schöier, F. L., Jansen, D. J., & van Dishoeck, E. F. 2007, A&A, 468, 627
Volk, K., & Cohen, M. 1990, AJ, 100, 2
Youngblood, A., France, K., Ginsburg, A., Hoadley, K., & Bally, J. 2018, ApJ, 857, 7
Zack, L. N., & Ziurys, L. M. 2013, ApJ, 765, 112
Zeigler, N. R., Zack, L. N., Woolf, N. J., & Ziurys, L. M. 2013, ApJ, 778, 16
Zhang, Y., Kwok, S., & Dinh-V-Trung 2008, ApJ, 678, 328
Zhang, Y., Kwok, S., & Dinh-V-Trung 2009, ApJ, 691, 1660
Ziurys, L. M., & Schmidt, D. R. 2024, in IAU Symp. 384, Planetary Nebulae: A Universal Toolbox in the Era of Precision Astrophysics, ed. O. De Marco, A. Zijlstra, & R. Szczerba (Cambridge: Cambridge Univ. Press) in press
Ziurys, L. M., Schmidt, D. R., & Woolf, N. J. 2020, ApJL, 900, L31
Ziurys, L. M., Tenenbaum, E. D., Pulliam, R. L., Woolf, N. J., & Milam, S. N. 2009, ApJ, 695, 1604